AIR-COUPLED DETECTION OF RAYLEIGH SURFACE WAVES TO ASSESS MATERIAL NONLINEARITY DUE TO PRECIPITATION IN ALLOY STEEL

A Thesis
Presented to
The Academic Faculty

by

Sebastian Thiele

In Partial Fulfillment
of the Requirements for the Degree
Master of Science in Engineering Science and Mechanics in the
School of Civil and Environmental Engineering

Georgia Institute of Technology
December 2013

AIR-COUPLED DETECTION OF RAYLEIGH SURFACE WAVES TO ASSESS MATERIAL NONLINEARITY DUE TO PRECIPITATION IN ALLOY STEEL

Approved by:

Professor Laurence J. Jacobs, Advisor
School of Civil and Environmental Engineering
Georgia Institute of Technology

Dr. Jin-Yeon Kim
School of Civil and Environmental Engineering
Georgia Institute of Technology

Dr. Jianmin Qu
Department of Civil and Environmental Engineering
Northwestern University

Date Approved: 20 August 2013

ACKNOWLEDGEMENTS

First, I would like to express my deepest appreciation to my advisor Professor Laurence J. Jacobs for the support and the highly motivative atmosphere he provided me during my time at Georgia Tech. Apart from making it possible to come to Atlanta and Georgia Tech he was always a helpful hand during the time I was working on this thesis and made it possible for me to go to QNDE conference in Baltimore, Md as well as to Oak Ridge National Lab.

I also would like to acknowledge Dr. Jin-Yeon Kim for his outstanding help and all the inspiring conversations we had. By sharing all his experience in the field of non-destructive evaluation he supported me and made this work possible. I really enjoyed working with him.

Furthermore I thank Dr. Jianmin Qu from Northwestern University for serving as a commitee member and reviewing this thesis.

Moreover I would like to acknowledge Dr. James Wall for giving valuable advice in the field of material science, especially for the discussions about formation of precipitates.

I would like to express my special thanks to Professor Lothar Gaul and Christian Ehrlich from the Institute of Applied and Experimental Mechanics at the University of Stuttgart for choosing me as a candidate for the ISAP Program, which is financially supported by the DAAD. The DAAD is gratefully acknowledged for supporting me with its scholarship.

Thanks goes to my labmates Katie Matlack, Gun Kim, Kevin Arne, David Torello, Chi-Won In, Mehdi Rashidi, Fabian Schempp and Merlin Morlock providing an engaging and motivating atmosphere in the lab. Special thanks thereby goes to Katie Matlack for her outstanding help and advice she gave me throughout the research project this thesis is based on. Additionally I would also like to acknowledge Fabian Schempp and Merlin Morlock for sharing joy and sorrow with me during our stay in Atlanta.

Special thanks goes also to all my friends in Germany, keeping in touch with me and helping

me whenever possible. Last but not least I would like to express my deepest gratitude to my family for supporting and motivating me throughout my time at Georgia Tech.

TABLE OF CONTENTS

LIST OF TABLES

LIST OF FIGURES

LIST OF SYMBOLS OR ABBREVIATIONS

Symbol	Description
a_s	source radius
A_n	wave amplitude
A_n^{el}	detected electrical amplitude of a wave
A_2^e, A_3^e	Huang coefficients
b_i	body force
$\mathbf{b}$	Burger's vector
B, D	amplitudes
c	wave velocity
c_L, c_T, c_R	longitudinal, transverse, Rayleigh wave velocity
C	tempering parameter
C_{ijkl}	forth order elastic tensor
C_{ijklmn}, M_{ijklmn}	higher order elastic tensor
$\mathbf{d}^{(n)}, \mathbf{d}$	unit vector in direction of motion
$\mathrm{d}s$	differential line segment
d_t	diameter of air-coupled transducer
$\mathbf{E}$	Lagrangian strain tensor
f_p	volume fraction precipitates
F	force
F_{ij}	deformation gradient
i	imaginary unit
$\mathbf{I}$	identity matrix
k_i	wavenumber
k_L, k_R	longitudinal, Rayleigh wavenumber
l_{air}	lift off distance
K	bulk modulus precipitate

Symbol	Description
m	mass
$\mathbf{n}, n_i$	unit normal vector
$\mathbf{p}^{(n)}, \mathbf{p}$	unit propagation vector
P, Q	elastic constants
R	conversion factor longitudinal-shear stress
r	radius dislocation line
r_0, r_1	initial, final radius precipitate
S	surface
S_d	area swept out by a dislocation
t	time
t_s	specimen thickness
T	dislocation line tension
$\mathcal{T}$	Temperature
t_i	traction
u_i	displacement
$\mathbf{u}^{(n)}, \mathbf{u}$	displacement vector
$\ddot{u}_i$	acceleration
v_s	wavespeed
V	volume
$\mathbf{x}, x_i$	Lagrangian coordinate
$\mathbf{x}^*, x_i^*$	Eulerian coordinate
$2L$	pinning distance dislocation line
α_n	attenuation coefficient
β	nonlinearity parameter
$\beta\prime$	relative nonlinearity parameter
β^{lat}	nonlinearity parameter due to lattice nonlinearity
β^{disloc}	nonlinear contribution of dislocation network
γ_d	shear strain

Symbol	Description
Γ_1	reference configuration
Γ_2	current configuration
δ	misfit parameter
δ_{ij}	Kronecker delta
ϵ	total strain
ϵ_e	elastic strain
ϵ_d	strain caused by dislocations
ϵ_{ij}	strain tensor
ε	actual misfit parameter
ω	angular frequency
Ω	conversion factor shear-longitudinal strain
$\phi_{n,0}$	phase
σ	longitudinal stress
σ_{ij}	Cauchy stress tensor
$\boldsymbol{\sigma}^{\mathrm{pk1}}, \sigma_{ij}^{\mathrm{pk1}}$	first Piola Kirchhoff stress tensor
ρ	density
τ	shear stress
λ, μ	Lame constants
θ_i	incident/reflection angle
ν	Poisson's ratio
Λ	wavelength
Λ_R	Rayleigh wavelength
$\Lambda^{(d)}$	dislocation density

SUMMARY

Nonlinear ultrasonic waves have demonstrated high sensitivities to various microstructural changes in metal including coherent precipitates; these precipitates introduce a strain field in the lattice structure. The thermal aging of certain alloy steels leads to the formation of coherent precipitates, which pin dislocations and contribute to the generation of a higher harmonics in an initially monochromatic wave.

The objective of this research is to develop a robust technique to perform nonlinear Rayleigh wave measurements in metals using a non-contact receiving transducer. In addition a discussion about the data processing based on the two-dimensional diffraction and attenuation model is provided in order to calculate the relative nonlinearity parameter.

A precipitate hardenable material, 17-4 PH stainless steel, is used to obtain different precipitation stages by thermal treatment and the influence of precipitates on the ultrasonic nonlinearity is assessed. Conclusions about the microstrucutural changes in the material are drawn based on the nonlinear Rayleigh surface wave measurement and complementary measurements of thermo-electric power, mircohardness and ultrasonic velocity. The results show that the nonlinearity parameter is sensitive to coherent precipitates in the material and moreover that precipitation characteristics can be characterized based on the obtained experimental data.

CHAPTER I

INTRODUCTION

1.1 Motivation and Objective

Material degradation of in alloy steels at elevated temperatures is often caused by the formation of precipitates, which leads to embrittlement and an increase in hardness. Many components in high temperature applications are critical for a safe operation and therefore a continuous evaluation throughout the lifetime of the changes in the material is necessary. A non-destructive evaluation technique to assess the hardening and embrittlement due to precipitation is therefore helpful to enable an operation longer than the actual lifetime and to reduce the replacement cost.

The material studied in this research is 17-4 PH stainless steel, one of the most common precipitate hardenable stainless steels, used in many applications in nuclear, chemical, and aerospace industry for reactor components, gears, jet engines and also in paper mills. The advantages of this material are its high strength, corrosion resistance, high ductility and hardenability. The hardening is caused by precipitation of copper-rich phases in the martensitic microstructure which has a high dislocation density.

It has been shown by Hikata et al. [13] that the pinning of dislocations leads to the generation of a second harmonic wave component in an initially monochromatic wave. This model has been extended by Cantrell et al. [7] to the case in which coherent precipitates introduce a stress field in the lattice, which pin dislocations, leading to second harmonic generation.

Nonlinear ultrasonic waves have shown to be sensitive to various types of microstructural changes such as low-cycle fatigue, which was investigated by Herrmann et al. [12] for a nickel-base superalloy and Walker et al. [39] for A36 steel using Rayleigh surface waves. Zeitvogel et al. [42] exploited the sensitivity of Rayleigh waves to near surface damage and showed the feasibility for detecting stress corrosion cracking in carbon steel. The effect of near

surface dislocations and residual stresses due to cold work introduced by shot-peening was monitored by Liu et al. [20] using nonlinear Rayleigh waves. A comprehensive study by Ruiz et al. [30] using various destructive and nondestructive measurement techniques showed the sensitivity of nonlinear waves to thermal aging of 2205 duplex steel, which leads to sigma phase precipitation. The hardening behavior of M250 maraging steel has been assessed by Viswanath et al. [35] using nonlinear bulk waves. Their study showed a correlation between very fine and coherent Ni_3Ti precipitates and the increase in second harmonic generation. A decrease in nonlinearity is observed in overaged stages which is due to the formation of reversed austenite and loss of coherency of the precipitates. Creep damage, which leads to the formation of voids, multi-poles, micro-cracks and macro-cracks has been investigated by Valluri et al. [34], observing a strong correlation between micro-voids and the nonlinear acoustic parameter. Recent studies by Matlack et al. [22] have proven the sensitivity of nonlinear waves to the rather complex damage mechanisms associated with neutron irradiation.

Moreover the sensitivity of nonlinear longitudinal waves to precipitates in the microstructure have been comprehensively investigated for ASTM A710 steel by Hurley et al. [18], observing a linear relation between the nonlinearity parameter and the measured inhomogeneous strain. The effect of coherency strain in aluminum 2024-T4 and the change in nonlinearity due to pinned dislocations was theoretically and experimentally studied by Cantrell and Yost [6].

Rayleigh surface waves, which are used in this research have the advantage, as compared to bulk and shear waves, that they only require access to one side of the component and additionally diffraction and attenuation effects are smaller and therefore Rayleigh waves travel long distances without significant loss of acoustic energy. These features make this type of wave ideal for non-destructive in-situ surveillance of complex components.

Contact-wedge transmitting and contact-wedge receiving setups have often been used ([42], [39], [20], [30], ...) to perform nonlinear Rayleigh surface wave measurements and have shown [42] to be time consuming and suffer from variations due to the inconsistent contact

conditions at the wedge-specimen interface, which makes this measurement technique inefficient. These circumstances has lead to the necessity to improve this technique and the usage of non-contact methods to make the measurement more flexible, less time consuming and more accurate. A Michelson interferometer detection setup to perform nonlinear Rayleigh wave measurements has been used by Hurley [17], which has the advantage to measure absolute displacement and enable to measure the Rayleigh wave field. Herrmann [12] provides a comprehensive study of a laser heterodyne interferometer detection setup for nonlinear Rayleigh wave measurements, emphasizing the necessity of high system linearity of the exciting system and the surface quality of the specimen. Recent studies by Cobb et al. [9] make use of electromagnetic acoustic transducers to perform fully non-contact nonlinear Rayleigh wave measurements, but do not achieve the desired consistency. We can conclude that non-contact methods have the advantage to be applicable to the in-situ measurement of specimens under hazardous or hostile conditions but still suffer from specimen surface conditions.

The objective of this research is to develop a more robust, accurate and flexible technique for the nonlinear Rayleigh wave measurement than the contact-wedge generation and detection setup, the desired technique should also be less dependent on the surface condition than already existing laser detection setups. Once this objective is achieved the nonlinearity of 17-4 PH stainless steel specimens in different precipitation stages are measured to investigate the influence of small copper-rich precipitates in steel on the second harmonic generation. Models relating the material microstructure and the second harmonic contribution due to precipitates are used to obtain information about the precipitation process. Thermo-electric power, hardness and ultrasonic velocity measurements are performed as well to provide additional data about the microstructural processes.

1.2 Structure of the Thesis

An introduction into the fundamentals of wave propagation will be given in Chapter 2 leading to the derivation of the basic characteristics of Rayleigh surface waves in a two dimensional half space. Moreover a brief explanation of the nonlinearity parameter β for

longitudinal waves and Rayleigh waves is provided. Chapter 3 discusses the phenomena of precipitation in metals and provides a derivation of the second harmonic generation due to pinned dislocations by precipitates. A brief discussion about the mircostructure of 17-4 PH steel, the material used in this research to investigate precipitation, is presented in Chapter 4 as well as the preparation of the specimens.

The experimental procedure of the nonlinear Rayleigh wave measurements using a non-contact air-coupled receiving transducer is presented in Chapter 5 and the results are compared with respect to the uncertainty with the contact-wedge receiving technique. In addition a discussion about the data processing obtained by the nonlinear ultrasonic measurement is provided, which shows an extension of the well known diffraction and attenuation model. The procedure of thermo-electric power, hardness and ultrasonic velocity measurements is briefly described in Chapter 6.

A discussion of the measurement results and the microstructural changes in the material is provided in Chapter 7. Finally Chapter 8 draws conclusions and gives an outlook for future work.

CHAPTER II

WAVE PROPAGATION IN ELASTIC SOLIDS

This chapter discusses the theoretical basics of wave propagation in solid materials based on the explanations of Achenbach [1] and Graff [10]. The introduction of plane waves and their reflection on a stress free surface leads to the introduction of Rayleigh surface waves. Furthermore wave propagation in an elastic solid with nonlinear stress-strain relationship will be discussed to derive the nonlinearity parameter, as an indicator of the material nonlinearity.

2.1 Cauchy's Equation of Motion

Beginning with Newton's first law

$$F_i = m\ddot{u}_i, \tag{1}$$

which has to hold for each arbitrary volume V with surface S in an elastic body of density ρ, we obtain

$$\int_S t_j \,\mathrm{d}S + \int_V \rho b_j \,\mathrm{d}V = \int_V \rho \ddot{u}_j \,\mathrm{d}V, \tag{2}$$

where t_j represents the traction acting on the boundary S of the volume V, b_j are the body forces and $\ddot{u}_j$ the second time derivative of the displacement. Using Cauchy's First Law, which relates the traction t_j acting on a surface with unit outward normal vector n_i to the Cauchy stress σ_{ij}

$$t_j = \sigma_{ij} n_i \tag{3}$$

the integral formulation (eqn. 2) yields

$$\int_S \sigma_{ij} n_i \,\mathrm{d}S + \int_V \rho b_j \,\mathrm{d}V = \int_V \rho \ddot{u}_j \,\mathrm{d}V, \tag{4}$$

which can be transformed to a volume integral using the divergence theorem

$$\int_V (\sigma_{ij,i} + \rho b_j - \rho \ddot{u}_j \,) dV = 0. \tag{5}$$

Since the volume that we are looking at can be arbitrarily small, one can obtain the local form of the equation of motion as

$$\sigma_{ij,i} + \rho b_j - \rho \ddot{u}_j \ = 0. \tag{6}$$

The general linear relation between the stress σ_{ij} and the strain ϵ_{kl} can be written using the elastic stiffness tensor C_{ijkl}

$$\sigma_{ij} = C_{ijkl}\epsilon_{kl}, \tag{7}$$

which simplifies for a homogeneous, isotropic material to

$$\sigma_{ij} = \lambda \epsilon_{kk}\delta_{ij} + 2\mu\epsilon_{ij} \tag{8}$$

with the Lamé constants

$$\lambda = \frac{E\nu}{(1+\nu)(1-2\nu)} \qquad \mu = \frac{E}{2(1+\nu)}, \tag{9}$$

where E represents the Young's modulus and ν the Poisson's ratio. By neglecting higher order terms and therefore applying linearized theory of deformation the strain-displacement relation becomes

$$\epsilon_{ij} = \frac{1}{2}(u_{i,j} + u_{j,i}), \tag{10}$$

which relates the strain tensor ϵ_{ij} and the displacements u_i. By using equations (6), (8) and (10) one can obtain the displacement based Navier equation of motion

$$\mu u_{j,ii} + (\lambda + \mu)u_{i,ij} + \rho b_j = \rho \ddot{u}_j, \tag{11}$$

which can be rewritten in vector notation neglecting body forces as

$$\mu \nabla^2 \mathbf{u} + (\lambda + \mu)\boldsymbol{\nabla}\boldsymbol{\nabla} \cdot \mathbf{u} = \rho \ddot{\mathbf{u}}. \tag{12}$$

If we take the divergence of this equation, it reduces to

$$(\lambda + 2\mu)\boldsymbol{\nabla}^2 \boldsymbol{\nabla} \cdot \mathbf{u} = \rho \boldsymbol{\nabla} \cdot \ddot{\mathbf{u}} \tag{13}$$

or

$$(\lambda + 2\mu)u_{i,ijj} = \rho \ddot{u}_{i,i}. \tag{14}$$

By identifying $\frac{\partial u_i}{\partial x_i}$ as the dilatation of the material and rewriting the equation with the simplification $\Delta = \frac{\partial u_i}{\partial x_i}$, we obtain

$$\frac{\partial^2 \Delta}{\partial t^2} = \frac{(\lambda + 2\mu)}{\rho} \frac{\partial^2 \Delta}{\partial x_j^2}. \tag{15}$$

This leads to the propagation velocity of volumetric or dilatational disturbances, which turns out to be

$$c_L = \sqrt{\frac{(\lambda + 2\mu)}{\rho}}. \tag{16}$$

If we take the curl of equation (12) and identify $\boldsymbol{\omega} = \frac{1}{2}\boldsymbol{\nabla} \times \mathbf{u}$ as the rotation vector we obtain

$$\frac{\partial^2 \boldsymbol{\omega}}{\partial t^2} = \frac{\mu}{\rho} \frac{\partial^2 \boldsymbol{\omega}}{\partial x_j^2}. \tag{17}$$

For this reason distorional or rotational waves propagate with the velocity

$$c_T = \sqrt{\frac{\mu}{\rho}}. \tag{18}$$

2.2 Linear Wave Propagation

2.2.1 Plane Waves in an Unbound Medium

The displacement vector $\mathbf{u}$ of a wave, which is propagating through an unbound medium with the velocity c in the direction of motion with the unit vector $\mathbf{d}$ can be expressed as

$$\mathbf{u} = f(\mathbf{x} \cdot \mathbf{p} - ct)\mathbf{d} \tag{19}$$

with the unit propagation vector $\mathbf{p}$ and the position vector $\mathbf{x}$. This equation describes a plane of constant phase normal to the propagation vector $\mathbf{p}$ for the condition $\mathbf{x} \cdot \mathbf{p} = \textit{constant}$. By substituting the plane wave equation (19) into Navier's equation of motion in absence of body forces (12) we obtain

$$(\mu - \rho c^2)\mathbf{d} + (\lambda + \mu)(\mathbf{p} \cdot \mathbf{d})\mathbf{p} = 0. \tag{20}$$

This equation can only be satisfied in two ways, either

$$\mathbf{d} = \pm \mathbf{p}, \tag{21}$$

which clearly represents a longitudinal wave or P-wave since the propagation vector $\mathbf{p}$ is parallel to the displacement vector $\mathbf{u}$ and the velocity comes out to be $c = c_L = \sqrt{\frac{(\lambda+2\mu)}{\rho}}$. The other possible solution is

$$\mathbf{p} \cdot \mathbf{d} = 0, \tag{22}$$

which is fulfilled if the unit vector in the direction of propagation $\mathbf{p}$ is perpendicular to the displacement vector $\mathbf{u}$. Hence we have established the particle motion of transverse waves or S-waves, leading to a phase velocity of $c = c_T = \sqrt{\frac{\mu}{\rho}}$.

For transverse waves we can clearly distinguish between two different types of waves, considering a two dimensional-plane (x_1, x_2-plane), where x_1 is the direction of wave propagation. For vertically polarized waves (SV-waves) the displacement vector is parallel to the x_2-direction and hence we have an in-plane displacement of the particles. Waves with an out-of-plane displacement, parallel to the x_3-direction are called horizontally polarized waves (SH-waves).

The wavenumber k_n of a wave n with the angular frequency ω_n and the propagating velocity c_n is defined as

$$k_n = \frac{\omega_n}{c_n}, \tag{23}$$

which is equal to the number of wavelengths Λ_n over 2π, implying

$$\Lambda_n = \frac{2\pi}{k_n}. \tag{24}$$

2.2.2 Reflection of Plane Waves at a Stress Free Surface

The displacement field of P- or SV-wave for the two dimensional case (x_1, x_2-plane) is denoted by

$$\mathbf{u}^{(n)} = A_n \mathbf{d}^{(n)} \exp\left[\mathrm{i}k_n(x_1 p_1^{(n)} + x_2 p_2^{(n)} - c_n t)\right], \tag{25}$$

where the index n is used to distinguish between the different occurring waves.

The reflection of an incident plane wave (either P- or SV-wave) with propagation vector $\mathbf{p}^{(0)}$ and wavenumber k_0 hitting a traction free boundary ($\sigma_{22} = \sigma_{21} = 0$) under the angle θ_0 (see Figure 2.1) induces in general a reflected P-wave and a reflected SV-wave. Figure 2.1(a) shows the angle θ_1 between the x_2-axis and the propagation vector of the reflected

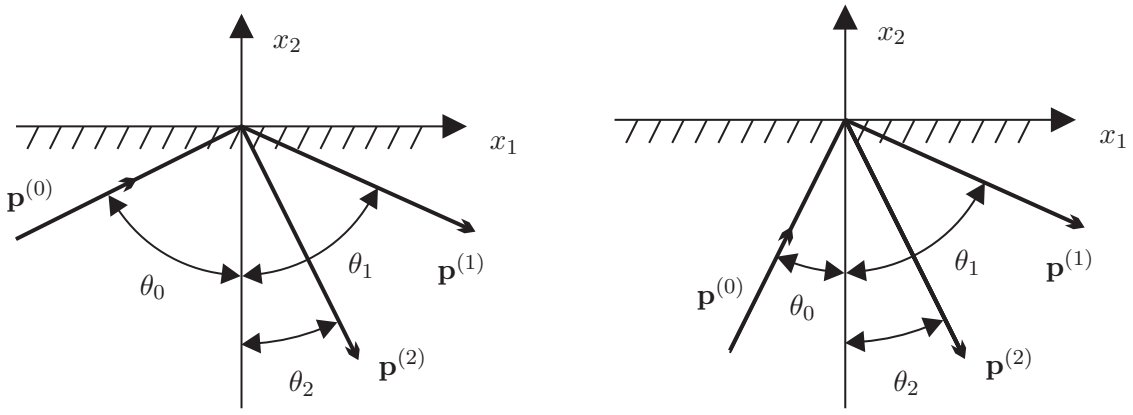

(a) Reflection of a P-wave

(b) Reflection of a SV-wave

Figure 2.1: Wave reflections on a free surface

P-wave (propagation vector $\mathbf{p}^{(1)}$ and wavenumber k_1), additionally the angle of reflection θ_2 of the SV-wave with propagation vector $\mathbf{p}^{(2)}$ and wavenumber k_2. For an incident P-wave with $\kappa = \left(\frac{2(1-\nu)}{1-2\nu}\right)^{\frac{1}{2}}$ we obtain

$$k_1 = k_0 \qquad k_2 = \frac{c_L}{c_T} k_0 = \kappa k_0 \tag{26}$$

$$\theta_1 = \theta_0 \qquad \sin\theta_2 = \kappa^{-1} \sin\theta_0. \tag{27}$$

The relationships for an incident SV-wave as shown in Figure 2.1(b) are

$$k_1 = \frac{c_T}{c_L} = \kappa^{-1} k_0 \qquad k_2 = k_0 \tag{28}$$

$$\sin\theta_1 = \kappa \sin\theta_0 \qquad \theta_2 = \theta_0. \tag{29}$$

2.3 Rayleigh Surface Waves

Rayleigh surface waves travel along a stress free boundary, which means the displacement decays exponentially with depth. For this reason the energy is concentrated at the surface of the elastic material.

2.3.1 Theory of Rayleigh Surface Waves

The displacements of a Rayleigh surface wave for the two-dimensional case of plane waves with wavenumber k_R can be described by a displacement field

$$u_1 = B\mathrm{e}^{-bx_2}\exp[\mathrm{i}k_R(x_1 - c_R t)] \tag{30a}$$

$$u_2 = D\mathrm{e}^{-bx_2}\exp[\mathrm{i}k_R(x_1 - c_R t)] \tag{30b}$$

$$u_3 = 0, \tag{30c}$$

where x_1 is the direction of propagation and c_R the phase velocity of the Rayleigh wave with the wavelength $\Lambda_R = 2\pi/k_R$. It is obvious that the parameter b has to be positive if x_2 denotes the axis pointing into the depth of the material to fulfill the requirement of a decreasing displacement amplitude for greater depth. This general displacement field certainly has to fulfill the displacement equation of motion (12), which leads to the equation

$$\left[c_L^2 b^2 - \left(c_L^2 - c_R^2\right) k_R^2\right]\left[c_T^2 b^2 - \left(c_T^2 - c_R^2\right) k_R^2\right] = 0, \tag{31}$$

representing the solution of the system of equations for nontrivial parameters B and D. Two constants

$$b_1 = k_R\left(1 - \frac{c_R^2}{c_L^2}\right)^{\frac{1}{2}} \qquad \text{and} \qquad b_2 = k_R\left(1 - \frac{c_R^2}{c_T^2}\right)^{\frac{1}{2}} \tag{32}$$

can be obtained from equation (31) leading to two different ratios for the constants B and D

$$\left(\frac{D}{B}\right)_1 = -\frac{b_1}{\mathrm{i}k_R} \qquad \left(\frac{D}{B}\right)_2 = \frac{\mathrm{i}k_R}{b_2}. \tag{33}$$

By substituting equations (32) and (33) into the displacement equations (30a) and (30b) we obtain

$$u_1 = \left[B_1\mathrm{e}^{-b_1 x_2} + B_2\mathrm{e}^{-b_2 x_2}\right]\exp[\mathrm{i}k_R(x_1 - c_R t)] \tag{34a}$$

$$u_2 = \left[-\frac{b_1}{\mathrm{i}k_R}B_1\mathrm{e}^{-b_1 x_2} + \frac{\mathrm{i}k_R}{b_2}B_2\mathrm{e}^{-b_2 x_2}\right]\exp[\mathrm{i}k_R(x_1 - c_R t)]. \tag{34b}$$

The stresses σ_{22} and σ_{21} have to vanish along the boundary $x_2 = 0$ to satisfy the boundary conditions, therefore B_1 and B_2 are related by

$$B_2 = -\frac{2b_1 b_2}{k_R^2 + b_2^2}B_1 \tag{35}$$

leading to a displacement field

$$u_1 = B_1 \left(\mathrm{e}^{-b_1 x_2} - \frac{2 b_1 b_2}{k_R^2 + b_2^2} \mathrm{e}^{-b_2 x_2} \right) \exp[\mathrm{i} k_R (x_1 - c_R t)] \tag{36a}$$

$$u_2 = \mathrm{i} B_1 \frac{b_1}{k_R} \left(\mathrm{e}^{-b_1 x_2} - \frac{2 k_R^2}{k_R^2 + b_2^2} \mathrm{e}^{-b_2 x_2} \right) \exp[\mathrm{i} k_R (x_1 - c_R t)]. \tag{36b}$$

Furthermore we obtain the equation for the phase velocity c_R of Rayleigh waves as

$$\left(2 - \frac{c_R^2}{c_T^2} \right)^2 - 4 \left(1 - \frac{c_R^2}{c_L^2} \right)^{\frac{1}{2}} \left(1 - \frac{c_R^2}{c_T^2} \right)^{\frac{1}{2}} = 0. \tag{37}$$

Since the wavelength Λ_R doesn't enter into this equation, we can conclude that Rayleigh waves are non-dispersive. For Poisson's ratios varying from 0 to 0.5 the approximation

$$c_R \approx \frac{0.862 + 1.14\nu}{1 + \nu} c_T \tag{38}$$

for the Rayleigh wave velocity c_R holds.

Since the displacement of Rayleigh waves decreases exponentially for greater depth a quantization is useful to make at this point. Based on the work of Achenbach [1] the thickness of the surface layer, undergoing non-negligible displacement, is approximately twice the wavelength Λ_R of the Rayleigh wave propagation in the half-space. The author plots the relative displacement $u_2(x_2)/u_2(0)$ over the ratio x_2/Λ_R and obtains for usual values of Poisson's ratio of metals $\nu = [0.25, 0.34]$ that the relative displacement approximately drops under 0.2 for $x_2/\Lambda_R = 1$, which means that most of the energy of the Rayleigh wave is located between $x_2 = 0$ and $x_2 = \Lambda_R$.

A particle directly located at the surface of an half-space in a Rayleigh wave displacement field undergoes an elliptical displacement, where the maximum amplitude of the displacement perpendicular to the surface $u_2^{\max}$ is approximately 1.5 times the maximum tangential displacement $u_1^{\max}$. The elliptical particle motion arises from the $\pi/2$-phase shift of u_1 and u_2. Figure 2.2 illustrates the particle motion in the surface for a Rayleigh wave propagating in an half-space.

2.4 Nonlinear Wave Theory

An ultrasonic wave propagating through an elastic solid generates higher harmonics due to the nonlinear distortion of the wave by the material. The measurement of the amplitude of

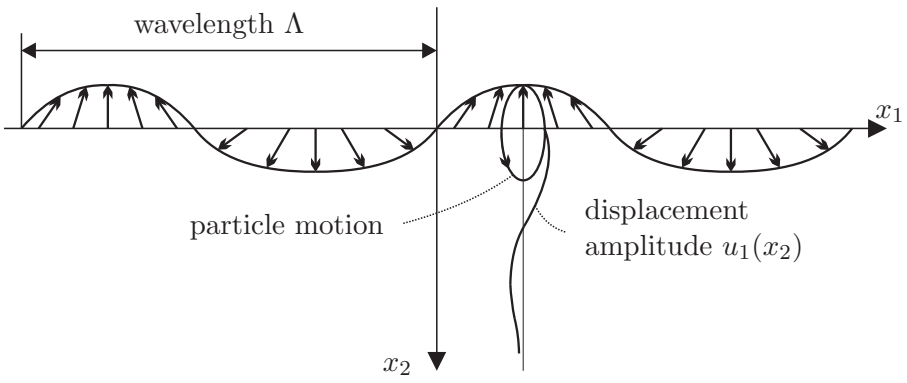

Figure 2.2: Displacement field of Rayleigh surface waves

these higher harmonics gives information about the nonlinearity of the medium. The non-dimensional acoustic nonlinearity parameter β, which will be introduced in section 2.4.1, relates the amplitudes of the propagating waves and gives therefore information about the nonlinearity of the stress-strain relation of the solid. The derivation of β for Rayleigh surface waves is discussed in section 2.4.2.

The practical applicability to microstructural arrangements has been shown by Hikata et al [13], who developed the contribution of dislocation structures to the nonlinearity parameter, this model has been further developed for sub-structural organization of dislocations by Cantrell [5]. Both models and their practical application will be introduced in section 3.3.

2.4.1 Nonlinearity Pararameter

The derivation for the equations of nonlinear wave propagation in an isotropic elastic medium is written based on the implementations of Hamilton and Blackstock [11]. According to equation (6), the wave motion in an elastic solid neglecting body forces can be written as

$$\rho \frac{\partial^2 u_i}{\partial t^2} = \sigma_{ij,j}, \tag{39}$$

where the particle displacement $\mathbf{u}$ denotes the vector from an initial point in the Lagrangian coordinate $\mathbf{x}$ to the same displaced point in the spatial or Eulerian coordinate $\mathbf{x}^*$ and is therefore defined as $u_i = x_i^* - x_i$. By introducing the deformation gradient tensor

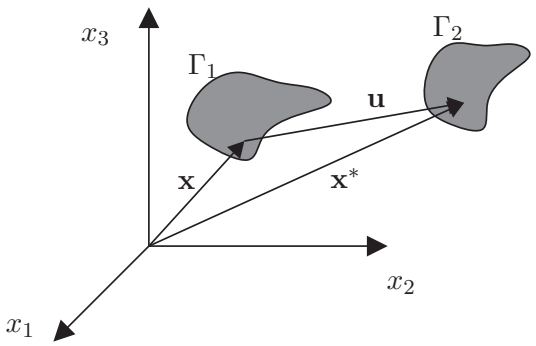

Figure 2.3: Body in the reference (Γ_1) and deformed (Γ_2) configuration

$$F_{ij} = \frac{\partial x_i^*}{\partial x_j}, \tag{40}$$

which represents the transformation from the reference to the deformed configuration, we obtain the Lagrangian strain tensor written in vector notation as

$$\mathbf{E} = \frac{1}{2}\left(\mathbf{F}^{\mathrm{T}} \cdot \mathbf{F} - \mathbf{I}\right) \tag{41}$$

or in indicial notation

$$E_{ij} = \frac{1}{2}\left(\frac{\partial u_i}{\partial x_j} + \frac{\partial u_j}{\partial x_i} + \frac{\partial u_k}{\partial x_i}\frac{\partial u_k}{\partial x_j}\right). \tag{42}$$

To be able to write equation (39) in terms of material coordinates, we introduce the non-symmetric first Piola-Kirchhoff stress tensor

$$\boldsymbol{\sigma}^{\mathrm{pk1}} = \left(\frac{\rho_0}{\rho}\right)\boldsymbol{\sigma} \cdot \mathbf{F}^{\text{-T}}. \tag{43}$$

Using equation (43) the Cauchy stress tensor can be written in terms of first Piola-Kirchhoff stress, which leads us, combining equation (43) and equation (39), to the equation of motion written in Lagrangian coordinates

$$\rho_0 \frac{\partial^2 u_i}{\partial t^2} = \frac{\partial \sigma_{ij}^{\mathrm{pk1}}}{\partial x_j}. \tag{44}$$

By exploiting that the specific strain energy per unit mass W depends only on local stretching and volume change and is therefore a function of the Lagrangian strain tensor, we obtain an expansion for small strain

$$\rho_0 W = \frac{1}{2}C_{ijkl}E_{ij}E_{kl} + \frac{1}{6}C_{ijklmn}E_{ij}E_{kl}E_{mn} + \dots . \tag{45}$$

With the relation between the first Piola-Kirchhoff stress and the strain energy

$$\sigma_{ij}^{\mathrm{pk1}} = \rho_0 F_{ik} \frac{\partial W}{\partial E_{kj}}, \tag{46}$$

we obtain

$$\sigma_{ij}^{\mathrm{pk1}} = C_{ijkl} \frac{\partial u_k}{\partial x_l} + \frac{1}{2} M_{ijklmn} \frac{\partial u_k}{\partial x_l} \frac{\partial u_m}{\partial x_n} + \dots , \tag{47}$$

where the higher order tensor can be rewritten as

$$M_{ijklmn} = C_{ijklmn} + C_{ijln}\delta_{km} + C_{jnkl}\delta_{im} + C_{jlmn}\delta_{ik}. \tag{48}$$

Combining equations (44) and (47) yields to the nonlinear wave equation

$$\rho_0 \frac{\partial^2 u_i}{\partial t^2} = \frac{\partial^2 u_k}{\partial x_j \partial x_l} \left(C_{ijkl} + M_{ijklmn} \frac{\partial u_m}{\partial x_n} + \dots \right). \tag{49}$$

This equation simplifies for a one-dimensional longitudinal wave propagating in x_1-direction using Voigt's notation for the second and third order elastic constants ($C_{ijklmn} = C_{IJK}$) to

$$\frac{\partial^2 u_1}{\partial t^2} = \frac{1}{\rho_0} \frac{\partial^2 u_1}{\partial x_1^2} \left(C_{11} + (C_{111} + 3C_{11}) \frac{\partial u_1}{\partial x_1} \right). \tag{50}$$

Moreover this equation can be rewritten in terms of the Huang coefficients using $A_2^e = C_1 + C_{11}$ and $A_3^e = C_{111} + 3C_{11}$, where C_1 denotes the initial stress. By setting the initial stress equal to zero we can write

$$\frac{\partial^2 u_1}{\partial t^2} = \frac{\partial^2 u_1}{\partial x_1^2} c_L^2 \left(1 + \frac{A_3^e}{A_2^e} \frac{\partial u_1}{\partial x_1} \right). \tag{51}$$

using the relationship $c_L^2 = \frac{A_2^e}{\rho_0}$,one can obtain the nonlinearity parameter

$$\beta = -\frac{A_3^e}{A_2^e} \qquad \text{for} \qquad \frac{\partial^2 u_1}{\partial t^2} = \frac{\partial^2 u_1}{\partial x_1^2} c_L^2 \left(1 - \beta \frac{\partial u_1}{\partial x_1} \right). \tag{52}$$

Furthermore it can be shown that for the nonlinear equation of motion in the one dimensional case

$$\rho_0 \frac{\partial^2 u_1}{\partial t^2} = \frac{\partial^2 u_1}{\partial x_1 \partial x_1} \left(P + Q \frac{\partial u_1}{\partial x_1} \right), \tag{53}$$

written in terms of a second order elastic constant P and the constant Q, which is a combination of second and third order elastic constants yields the nonlinearity parameter as

$$\beta = -\frac{Q}{P}. \tag{54}$$

Note that this equation will be useful in the derivation of the second harmonic contribution due to dislocation substructures in Section 3.3. For an excitation with a harmonic wave of amplitude A and frequency ω, having a displacement field of form

$$u_1 = Acos(kx_1 - \omega t), \qquad \text{with} \qquad k = \frac{\omega}{c_L} \tag{55}$$

we obtain

$$\begin{aligned} u_1 &= A_1 cos(kx_1 - \omega t) + A_2 cos(2kx_1 - 2\omega t) + \dots \\ &= A_1 cos(kx_1 - \omega t) + \frac{1}{8}\beta k^2 A_1^2 X_1 cos(2kx_1 - 2\omega t) + \dots , \end{aligned} \tag{56}$$

as a solution of the nonlinear wave equation (50). Therefore we can express the acoustic nonlinearity parameter β in terms of the amplitudes of the fundamental and second harmonic wave as

$$\beta = \frac{A_2}{A_1^2}\frac{8c_L^2}{\omega^2 x_1}. \tag{57}$$

2.4.2 Nonlinearity of Rayleigh Surface Waves

If we recall a Rayleigh wave propagating in the x_1 direction, where the x_2 direction is pointing into depth of an elastic half space, the displacement field $u_i(\omega)$ of the fundamental wave is given by

$$u_1(\omega) = A_1 \left(\mathrm{e}^{-b_1 x_2} - \frac{2b_1 b_2}{k_R^2 + b_2^2} \mathrm{e}^{-b_2 x_2} \right) \exp[\mathrm{i}k_R(x_1 - c_R t)] \tag{58a}$$

$$u_2(\omega) = \mathrm{i}A_1 \frac{b_1}{k_R} \left(\mathrm{e}^{-b_1 x_2} - \frac{2k_R^2}{k_R^2 + b_2^2} \mathrm{e}^{-b_2 x_2} \right) \exp[\mathrm{i}k_R(x_1 - c_R t)]. \tag{58b}$$

As shown by Herrmann et al [12] the displacement field $u_i(2\omega)$ of the second harmonic Rayleigh wave can be written for a material with weak quadratic nonlinearity at sufficiently large distances as

$$u_1(2\omega) \approx A_2 \left(\mathrm{e}^{-2b_1 x_2} - \frac{2b_1 b_2}{k_R^2 + b_2^2} \mathrm{e}^{-2b_2 x_2} \right) \exp[\mathrm{i}2k_R(x_1 - c_R t)] \tag{59a}$$

$$u_2(2\omega) \approx \mathrm{i}A_2 \frac{b_1}{k_R} \left(\mathrm{e}^{-2b_1 x_2} - \frac{2k_R^2}{k_R^2 + b_2^2} \mathrm{e}^{-2b_2 x_2} \right) \exp[\mathrm{i}2k_R(x_1 - c_R t)], \tag{59b}$$

where u_1 is the longitudinal, u_2 the shear contribution of the wave. Since the third order elastic constants vanish for a shear deformation in an isotropic material the generation of

second harmonic components is solely due to longitudinal deformation. We are therefore able to write the nonlinearity parameter, which relates the amplitudes of first and second harmonic for a Rayleigh wave in terms of the vertical displacements at the surface $u_2(x_2 = 0) = \bar{u}_2$ by combining equations (57), (58b) and (59b), which yields

$$\beta = \frac{\bar{u}_2(2\omega)}{\bar{u}_2^2(\omega)} \frac{\mathrm{i}8b_1}{k_L^2 x_1 k_R} \left(1 - \frac{2k_R^2}{k_R^2 + b_2^2}\right). \tag{60}$$

CHAPTER III

PECIPITATION HARDENING

3.1 Introduction

Thermal aging of certain alloy steels causes the formation precipitates when a certain alloy element is initially supersaturated in the lattice structure. The formation of sub-microscopic copper-rich precipitates can be observed during the heat treatment of precipitate hardenable materials as well as the aging of some steels. Precipitates impede the movement of dislocations in the matrix leading to an increase in hardness. The precipitation process is enhanced due to the higher diffusion rate of the alloying element at higher temperatures, which causes the dispersively distributed copper to form precipitates in the matrix.

However the formation of precipitates is not always desirable. Thermal embrittlement of an alloy steel is often caused by the formation of precipitates leading a degradation of the material at elevated temperatures over time. The thermal embrittlement in 2205 duplex stainless steel has been investigated using nonlinear Rayleigh surface waves by Ruiz et al. [30]. Furthermore the embrittlement due to radiation damage is partly caused by small copper-rich precipitates which form because of the enhanced diffusion due to vancany clusters and elevated temperatures. The small vacancy clusters lead to relatively small copper-rich precipitates with a diameter between 1.5 and 3 nm as reported by Odette et al. [24].

3.2 Theoretical Background

This section will give a brief introduction to the microstructural changes of precipitation, based on the comprehensive explanations of Martin [21]. The book is also recommended to the interested reader to grasp a broader knowledge on the mechanisms of precipitation than this section can provide.

Precipitation hardening in steel is driven by the reduction of the total Gibbs free energy of the system. However a thermodynamic nucleation barrier has to be overcome in order for

the precipitation process to start. The nucleation starts therefore often at grain boundaries, dislocations or inclusions, where the Gibbs free energy of the atoms is generally higher, leading to a heterogeneous nucleation. Furthermore higher temperatures help to overcome the thermodynamic barrier by increasing the Gibbs free energy. The crystal structure and the lattice parameters of the alloy atoms and the matrix material determine if the nucleation and growth of the precipitates is either coherent or incoherent. The growth of precipitates is driven by the diffusion of the alloying element in the matrix and interface reactions. The diffusion rate is high in the early stages of precipitate growth because of high concentration gradient in the material directly surrounding the precipitate. However it drops for later stages of precipitate growth leading to a slow down. The increase of the volume fraction of precipitates stops, when the matrix can fully dissolve the remaining alloying element, obtaining a matrix, which is saturated with the alloying element. Further growth of precipitates is only caused by coarsening, which lowers the interfacial energy between the matrix and the precipitates, however, the total volume fraction of precipitates remains constant.

3.3 Nonlinearity Due to Precipitation

Based on the fundamental achievements of Hikata et al. [13], who describe the change in the nonlinearity parameter due to a dislocation pinned at two points, Cantrell et al. [7] have developed a model which relates the change in the nonlinearity parameter with the volume fraction and the average radius of the precipitates. The following considerations will derive this relationship based on the models mentioned being slightly adjusted at some points and for some parts an extended derivation is provided.

A dislocation, which is pinned at two points with a distance $2L$ apart from each other, can be bowed out by a shear stress τ as depicted in Figure 3.1 causing the dislocation line to form an arc with radius r and angle 2ϕ. The shear stress is caused by a static longitudinal stress σ and can be calculated using the conversion factor R from longitudinal to shear stress, yielding $\tau = R\sigma$. The dislocation line tension can be expressed in terms of the

magnitude of the Burger's vector $\mathbf{b}$ and the shear modulus μ and can be written as

$$T = \frac{1}{2}\mu \left|\mathbf{b}\right|^2 . \tag{61}$$

As shown in Figure 3.2, the force T acts on both sides of the differential line segment $\mathrm{d}s$

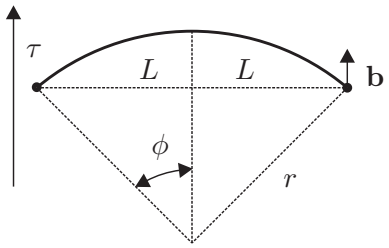

Figure 3.1: Dislocation line undergoing shear stress

and the projected force F towards the center of the arc can be written as $F = 2T\sin(\phi)$, which simplifies for a small angle ϕ to $F = 2T$. With the relation $\sin(\phi) = \frac{\mathrm{d}s/2}{r}$ we can express the force F as

$$F = 2T\frac{\mathrm{d}s/2}{r} = \frac{T\mathrm{d}s}{r}. \tag{62}$$

Approximating the dislocation to be bowed out by the order of the length of the Burger's vector we obtain $F = \tau \left|\mathbf{b}\right| \mathrm{d}s$. Using equations (61) and (62) we can write

$$\tau = \frac{\mu \left|\mathbf{b}\right|^2}{2 \left|\mathbf{b}\right| r} = \frac{\mu \left|\mathbf{b}\right|}{2r}. \tag{63}$$

Generally the shear strain caused by a dislocation network can be written as

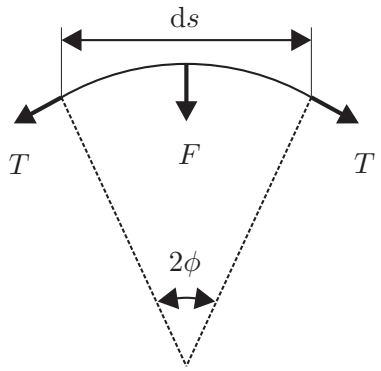

Figure 3.2: Dislocation line under line tension

$$\gamma_d = \Lambda^{(d)} |\mathbf{b}| \, \overline{x}, \tag{64}$$

where $\Lambda^{(d)}$ denotes the dislocation density and $\overline{x}$ the average distance the dislocation has moved. According to Figure 3.1 the average distance the dislocation has moved can be written as $\overline{x} = S_d/2L$, where S_d denotes the area swept out by the dislocation. This area can be calculated to

$$S_d = r^2 \left(\phi - \frac{1}{2} \sin(2\phi) \right), \tag{65}$$

Using equations (63), (64) and (65) Hikata et al. [13] obtain γ_d as

$$\gamma_d = \frac{2}{3} \frac{\Lambda^{(d)} L^2}{\mu} \tau + \frac{4}{5} \frac{\Lambda^{(d)} L^4}{\mu^3 |\mathbf{b}|^2} \tau^3 \tag{66}$$

or in terms of the longitudinal stress

$$\gamma_d = \frac{2}{3} \frac{\Lambda^{(d)} L^2 R}{\mu} \sigma + \frac{4}{5} \frac{\Lambda^{(d)} L^4 R^3}{\mu^3 |\mathbf{b}|^2} \sigma^3. \tag{67}$$

Since due to the longitudinal stress σ the material undergoes an elastic strain ϵ_e, therefore the total strain can be written as

$$\epsilon = \epsilon_e + \epsilon_d, \tag{68}$$

where ϵ_d denotes the strain contribution of the network of bowed out dislocations in the material. If we express the stress due to the longitudinal strain using a similar approach as in equation (47) retaining the first two terms of a power series expansion with A_2^e and A_3^e being the second and third order Huang coefficients respectively, we obtain

$$\sigma = A_2^e \epsilon_e + \frac{1}{2} A_3^e \epsilon_e^2 \tag{69}$$

or

$$\epsilon_e = \frac{1}{A_2^e} \sigma - \frac{1}{2} \frac{A_3^e}{(A_2^e)^3} \sigma^2. \tag{70}$$

By plugging equation (70) and (67) into equation (68) using Ω, the factor converting the shear strain γ_d to longitudinal strain ϵ_d we can write the total strain ϵ, the material is undergoing as

$$\epsilon = \left(\frac{1}{A_2^e} + \frac{2}{3} \frac{\Lambda^{(d)} L^2 R \Omega}{\mu} \right) \sigma - \frac{1}{2} \frac{A_3^e}{(A_2^e)^3} \sigma^2 + \frac{4}{5} \frac{\Lambda^{(d)} L^4 R^3 \Omega}{\mu^3 |\mathbf{b}|^2} \sigma^3. \tag{71}$$

The inversion of this relation is based on the explanations of Cantrell [4], where he uses a Taylor series expansion centered at an initial stress σ_0, which causes an initial strain ϵ_0. By increasing the initial stress by infinitesimal stress $\Delta\sigma$, causing an additional strain $\Delta\epsilon$ we obtain the total stress as $\sigma = \sigma_0 + \Delta\sigma$, which can be written as

$$\begin{aligned}\sigma &= \sigma_0 + \left(\frac{\partial\sigma}{\partial\epsilon}\right)\Delta\epsilon + \frac{1}{2}\left(\frac{\partial^2\sigma}{\partial\epsilon^2}\right)\Delta\epsilon^2 \\ &= \sigma_0 + \left(\frac{\partial\epsilon}{\partial\sigma}\right)^{-1}\Delta\epsilon - \frac{1}{2}\left[\left(\frac{\partial^2\epsilon}{\partial\sigma^2}\right)\left(\frac{\partial\epsilon}{\partial\sigma}\right)^{-3}\right]\Delta\epsilon^2\end{aligned} \tag{72}$$

or

$$\begin{aligned}\Delta\sigma &= \left(\frac{\partial\epsilon}{\partial\sigma}\right)^{-1}\Delta\epsilon - \frac{1}{2}\left[\left(\frac{\partial^2\epsilon}{\partial\sigma^2}\right)\left(\frac{\partial\epsilon}{\partial\sigma}\right)^{-3}\right]\Delta\epsilon^2 \\ &= P\Delta\epsilon + \frac{1}{2}Q\Delta\epsilon^2.\end{aligned} \tag{73}$$

Therefore we obtain

$$P = \left(\frac{\partial\epsilon}{\partial\sigma}\right)^{-1} = \left(\frac{1}{A_2^e} + \frac{2}{3}\frac{\Lambda^{(d)}L^2R\Omega}{\mu} - \frac{A_3^e}{\left(A_2^e\right)^3}\sigma + \frac{12}{5}\frac{\Lambda^{(d)}L^4R^3\Omega}{\mu^3\left|\mathbf{b}\right|^2}\sigma^2\right)^{-1}, \tag{74}$$

which simplifies to

$$P = \left(\frac{1}{A_2^e} + \frac{2}{3}\frac{\Lambda^{(d)}L^2R\Omega}{\mu}\right)^{-1}, \tag{75}$$

since σ is usually of the order of MPa and for this reason the terms multiplied by σ can be neglected compared to the terms involving the Huang coefficient A_2^e and the shear modulus μ, which are at the order of GPa. Furthermore we obtain

$$Q = \left(\frac{A_3^e}{\left(A_2^e\right)^3} - \frac{24}{5}\frac{\Lambda^{(d)}L^4R^3\Omega}{\mu^3\left|\mathbf{b}\right|^2}\sigma_0\right)\left(\frac{1}{A_2^e} + \frac{2}{3}\frac{\Lambda^{(d)}L^2R\Omega}{\mu}\right)^{-3}, \tag{76}$$

which leads to the nonlinearity parameter due to the relationship obtained in equation (54) for the most general case

$$\beta = -\frac{Q}{P} = \frac{\left(-\frac{A_3^e}{\left(A_2^e\right)^3} + \frac{24}{5}\frac{\Lambda^{(d)}L^4R^3\Omega}{\mu^3\left|\mathbf{b}\right|^2}\sigma_0\right)}{\left(\frac{1}{A_2^e} + \frac{2}{3}\frac{\Lambda^{(d)}L^2R\Omega}{\mu}\right)^2}. \tag{77}$$

It can be shown that the second term $\frac{\Lambda^{(d)}L^2R\Omega}{\mu}$ in equation (75) can be neglected compared to the first term $\frac{1}{A_2^e}$ and therefore equation (77) can be simplified to

$$\beta = \left(-\frac{A_3^e}{A_2^e} + \frac{24}{5}\frac{\Lambda^{(d)}L^4R^3\Omega\left(A_2^e\right)^2}{\mu^3\left|\mathbf{b}\right|^2}\sigma_0\right), \tag{78}$$

where we can clearly identify the second harmonic generation contribution of the lattice structure due to the nonlinear stress strain relationship

$$\beta^{lat} = -\frac{A_3^e}{A_2^e} \tag{79}$$

and the contribution of the network of pinned dislocations

$$\beta^{disloc} = \frac{24}{5}\frac{\Lambda^{(d)} L^4 R^3 \Omega \left(A_2^e\right)^2}{\mu^3 \left|\mathbf{b}\right|^2}|\sigma_0|, \tag{80}$$

If we consider an unconstrained precipitate with radius $r_0(1+\delta)$ inserted into a hole in the lattice structure with radius r_0, the final radius of the precipitate r_1 can be derived according to Martin [21], using the the bulk modulus K of the precipitate, the shear modulus μ of the lattice and the actual misfit parameter ε, yielding

$$r_1 = r_0(1+\varepsilon) \qquad \varepsilon = \frac{3K}{3K+4\mu}\delta. \tag{81}$$

The radial stress field $\sigma(r)$ of a spherical precipitate with a final radius r_1 introduced in the lattice structure can therefore be written as

$$\sigma(r) = -\frac{4\mu\varepsilon r_1^3}{r^3}. \tag{82}$$

By evaluating the stress at the midpoint $r = \frac{\mathrm{L}}{2}$, between two precipitates, as depicted in Figure 3.3 where the local stress results from the superposition of both radial stress fields, we obtain

$$\sigma_0 = -\frac{64\mu\varepsilon r_1^3}{L^3}, \tag{83}$$

which yields the change in the nonlinearity parameter based on equation (80) and (81) as

$$\beta^{disloc} = 307.2\frac{\Lambda^{(d)} L R^3 \Omega \left(A_2^e\right)^2 r_1^3}{\mu^2 \left|\mathbf{b}\right|^2}\frac{3K}{3K+4\mu}|\delta|. \tag{84}$$

For practical application it is useful to relate the change in nonlinearity due to precipitation to the volume fraction of precipitates in the material. Cantrell et al. [7] relate the average actual radius of the precipitate r_1 and the average distance L between two precipitates to the volume fraction f_p and obtains

$$L = \frac{2r_1}{\sqrt[3]{f_p}}, \tag{85}$$

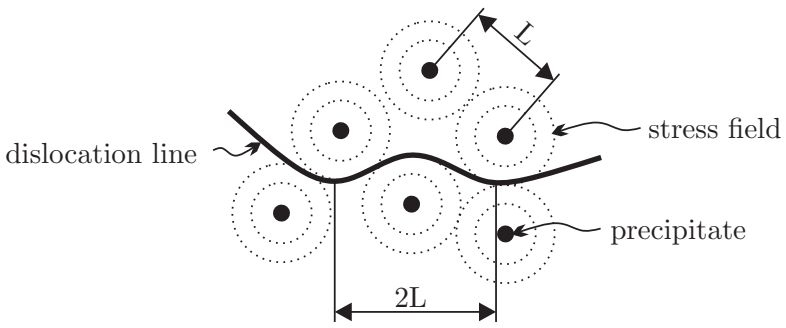

Figure 3.3: Dislocation line in precipitate network

which can be plugged into equation(84) to obtain the nonlinear contribution in terms of the volume fraction and average radius of precipitates.

Note that equation (84) and (85) can be used to obtain information about the microstructure of a material which contains precipitates based on the macroscopic nonlinear ultrasonic measurement. This model can therefore be very helpful in evaluating the precipitation kinetics of various materials.

CHAPTER IV

MATERIAL

4.1 17-4 PH Stainless Steel

The material used in this research, 17-4 PH, is one of the most common precipitate hardenable stainless steels, with a material composition shown in Table 4.1. The commercially purchased material has a tensile strength of 1384 N/mm^2 and a yield strength of approximately 1263 N/mm^2. The material is hot rolled and solution annealed at 1040°C for 6h, following an air cooling process, as it is received from the manufacturer.

Table 4.1: Material composition of 17-4 PH stainless steel specimens

17-4 PH - Chemical composition in wt.%									
C	0.023	Si	0.460	Mn	0.630	P	0.016	S	0.001
Cr	15.150	Ni	4.460	Mo	0.080	Co	0.044	Cu	3.070
N	0.023	Ti	0.001	Nb	0.260	Ta	0.000		

It has been reported that austenitised 17-4 PH stainless steel as it cools down starts to form martensite at 160°C (M_s) [8]. Moreover the dislocation density in martensite and austenite increases due to the shear deformation and volume expansion during the transformation leading to the high mechanical properties and a martensite fraction above 95% at room temperature. 17-4 PH stainless steel has been shown [8] to have a constant dislocation density of approximately $4 \times 10^{15} m^{-2}$, when it is heated up from room temperature to 500°C. Moreover no phase change from martensite to austenite has been seen during the heating process below 600°C. These properties allow a heat treatment of this material below 500°C without changing the dislocation density or the phase, which is important for the later evaluation of the nonlinear results since the nonlinear contribution due to precipitate pinned dislocations is dependent on the dislocation density.

4.2 Precipitation Kinetics

The microstructure in the unaged state of 17-4 PH steel is a martensite matrix, where approximately 3 wt.% of copper are dissolved in, this solid solution is supersaturated below temperatures of $\sim 925°C$ [32]. The copper precipitation in 17-4 PH steel is coherent in the beginning since copper and iron are similar in terms of their atomic radii and structure. However, in later stages of precipitation, especially in the phase of coarsening, Viswanathan et al. [36] observed that the precipitates are loosing their coherency. The incoherency of the precipitates is indicated by the loss of their spherical shape and the absence of a stress field around the precipitates.

Hsiao et al. [15] observed coherent, body-centered cubic (bcc) elliptical precipitates in 17-4 PH stainless steel reaching a size of approximately 25nm x 15nm in the peak hardening stage, by heat treating the specimen at 480°C for 1h. Moreover they reports the loss of coherency of the precipitates in later stages of precipitation, leading to a subsequent decrease in hardness. These incoherent precipitates are copper rich clusters with a face-centered cubic (fcc) lattice structure. A similar precipitate size in the peak hardening stage has also been observed by Viswanathan et al. [36], who report an average particle size of 15nm of copper rich precipitates.

4.3 Specimen Preparation

The specimens are received from the manufacturer having a thickness of 19 mm, a width of 38 mm, and a length of 230 mm. Smooth and parallel surfaces are obtained by surface grinding the two opposite sides of the specimen, where the Rayleigh wave measurements are performed. All specimens are surface grinded after the solution annealing and cooling; either air cooling or water quenching. The specimens are continuously cooled during the surface grinding to avoid heating and only a layer of approximately 0.013 mm thickness is taken off per cut in order to minimize effects on the surface microstructure during the grinding of the samples. The samples are hand polishing after the grinding in order to remove all visible texture effects introduced by the surface grinding.

The heat treatment schedule (Table 4.2) was chosen to obtain several precipitation

stages of the material based on the comprehensive overview of the hardening behavior of 17-4 PH stainless steel given by Mirzadeh et al. [23] who fit a curve to the experimental data obtained by many authors and plots it over the non-dimensional tempering parameter P and thereby obtains a master curve for the increase in hardness for various heat treatment temperatures.

Two samples (SA-AC #1 and SA-AC #2) in the solution annealed and air cooled state are used as reference samples to investigate the variation between two samples, which are identically treated. Three samples, which were solution annealed and air cooled are treated for various heat treatment duration to obtain different precipitation stages in the pre-peak hardening range. The maximum increase in hardness which is achievable with 17-4 PH stainless steel depends on the sample and varies between 15% and 45%. However the mean value calculated by Mirzadeh et al. [23] suggest an average increase in hardness of 30% in the peak hardening stage compared to the unaged state and this value is used as a baseline.

Table 4.2: Heat treatment schedule of specimens

	Solution annealing		Thermal aging		
Sample	Temperature [°C]	Cooling	Temperature [°C]	Time [h]	Tempering parameter P
SA-WQ	1040	water quenched	-	-	-
SA-WQ 400-1.0			400	1.0	13.5
SA-AC #1		air cooled	-	-	-
SA-AC #2			-	-	-
SA-AC 400-0.1			400	0.1	11.9
SA-AC 400-1.0			400	1.0	13.5
SA-AC 400-6.0			400	6.0	14.7

The tempering parameter for aging introduced by Hollomon-Jaffe [14] for the samples is chosen based on the results of Mirzadeh et al. [23] for the three solution annealed and air cooled samples which are aged. An increase in hardness of 12% (SA-AC 400-0.1), 20% (SA-AC 400-1.0) and 27% (SA-AC 400-6.0) is intended with the heat treatment in order to obtain precipitation stages which cover the range from the unaged state to the peak hardening stage. Temperature and time of the heat treatment are chosen in order to obtain

reasonable heat treatment times at a temperature well below the critical temperature of 500°C where the dislocation density starts [8] to decrease. The tempering parameter P can be calculated using

$$P = \mathcal{T}(C + \log(t)) \times 10^{-3}, \tag{86}$$

where $\mathcal{T}$ represents the temperature in Kelvin, t the time in hours and C is a material dependent constant, which is chosen to be 20 for 17-4 stainless steel by Mirzadeh et al. [23]. All samples are placed in the cool furnace and heated up with the heating rate of the furnace. A thermocouple is used to monitor the temperature of the specimen and the actual heat treatment time starts, when the sample reaches the specified temperature.

The oxidized layer which forms during the heat treatment is removed by polishing the surface using 400 grid sand paper to obtain the same surface condition as the reference samples.

Two specimens are solution annealed and water quenched in addition to the solution annealed and air cooled samples because a significant decrease in hardness can be observed [15] after solution annealing and water quenching compared to subsequent air cooling. In addition one of the water quenched sample is aged at 400°C for 1 h in order to be able to compare the aging behavior after water quenching with the hardening after air cooling.

CHAPTER V

NONLINEAR RAYLEIGH WAVE MEASUREMENT USING AIR-COUPLED-RECEIVER

The nonlinear air-coupled-detection Rayleigh wave measurement setup (Figure 5.1) consists of one narrow band piezoelectric transducers, exciting a longitudinal wave, which is introduced in a plexiglas wedge to excite a Rayleigh surface wave in the specimen. A sinusoidal tone bust with 2.1 MHz is used for the excitation of the transducer. The desired high-voltage excitation signal for the transducer is obtained by amplifying the output signal of the function generator with the RITEC GA-2500A high power gated amplifier. The receiving air-coupled transducer centered at 3.9 MHz receives the longitudinal wave in air, which is leaked by the Rayleigh wave. The obtained output signals are post amplified to improve the signal-to-noise ratio and the signals are recorded and averaged by an oscilloscope.

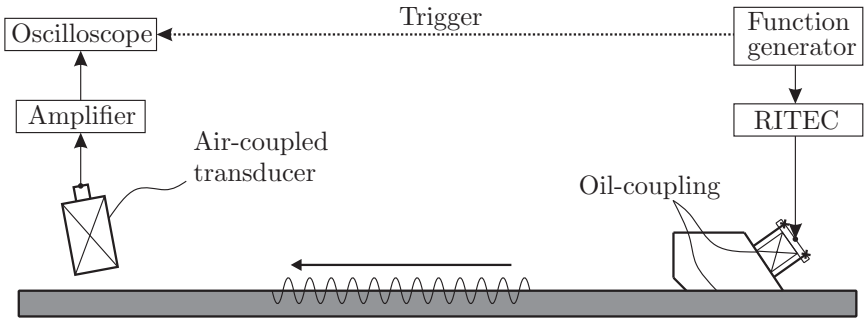

Figure 5.1: Experimental setup using non-contact air-coupled receiver

5.1 Setup Components

5.1.1 Function Generator

A function generator is used to obtain a sinusoidal signal at the excitation frequency of 2.1 MHz with a peak to peak voltage of 800 mV. The source signal consists of 20 cycles and provides therefore a sufficiently long steady state portion, which is important for the subsequent signal processing. The internal trigger of the function generator is used to

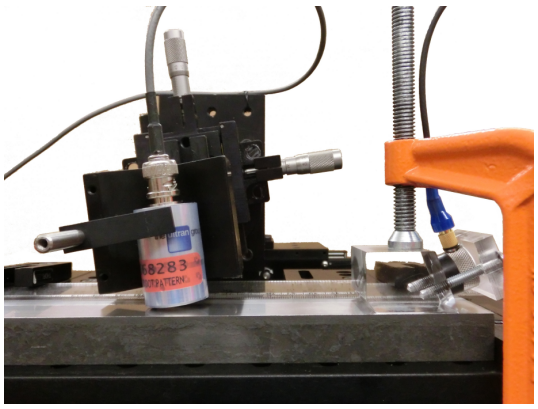

Figure 5.2: Air-coupled transducer and wedge mounted on the sample

synchronize the source with the amplifier and the oscilloscope.

5.1.2 High Power Gated Amplifier

A high power amplifier (RITEC GA-2500A) provides a sufficient high-voltage excitation signal for the the narrow band transducer used for the excitation. A high excitation signal is desirable to introduce waves with high enough acoustic energy and therefore ensuring a good signal-to-noise ratio for the second harmonic component at the receiver. This type of amplifier provides a very clean output signal and introduces only a very small amount of inherent nonlinearity. The device has to be turned on for 30 minutes before the actual measurement in order to warm up and thereby ensuring a stable output signal during the measurement.

5.1.3 Transducers

A Panametrics V-type piezoelectric half inch narrow band transducer with a nominal frequency of 2.25 MHz is used for excitation and converts the electrical input signal into a longitudinal wave in the wedge. The frequency response of the exciting transducer is depicted in Figure 5.3(a).

The center frequency of the receiving transducer needs to be tuned around the frequency of the second harmonic wave to get the highest sensitivity at that frequency. The transducer

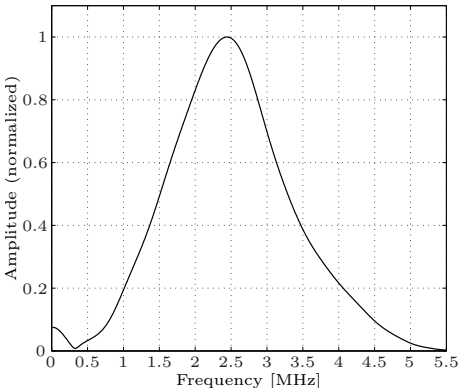

(a) Frequency response of the exciting Panametrics V-type piezoelectric transducer

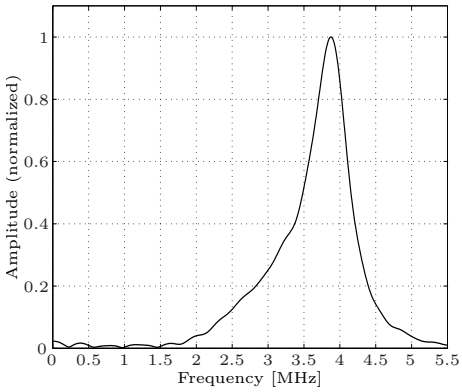

(b) Frequency response of the Ultran NCT4-D13 air-coupled transducer, obtained based on the reflection from a flat target with 2 mm lift off distance

Figure 5.3: Frequency response of the exciting and receiving transducer

converts the received ultrasonic wave into a electrical signal. An Ultran NCT4-D13 air-coupled transducer with a nominal frequency of 4 MHz is used in this research to detect the leaked longitudinal wave in air. The transducer is actually centered at 3.9 MHz (Figure 5.3(b)) and has an active area with a diameter of 12.5mm.

5.1.4 Rayleigh Wave Wedge

By introducing a longitudinal wave into a plexiglas wedge we are able to generate a Rayleigh surface wave in the specimen based on Snell's law. The angle θ_w as depicted in Figure 5.4 can be calculated using the wave speed $c_P^{(wedge)}$ of a longitudinal wave in the wedge material and $c_R^{(sample)}$ the Rayleigh wave speed in the sample as

$$\theta_w = arcsin\left(\frac{c_P^{(wedge)}}{c_R^{(sample)}}\right). \tag{87}$$

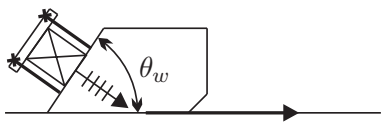

Figure 5.4: Wedge geometry

An acoustic coupling between the wedge and the sample is achieved by light lubrication

oil, the same oil ensures also the coupling between transducer and wedge. A good contact between the wedge and the sample has to be ensured throughout all measurements and the surface condition of the sample is therefore essential to obtain consistent results. Also the force which clamps the wedge down to the sample, affects the measurement and needs to be consistent in all measurements. Moreover settling effects can be seen, which means that the measured amplitude of the wave changes right after clamping the wedge as shown by Walker [38]. This phenomena is caused by the oil at the wedge-specimen interface, which is partly and slowly squeezed out of the contact area, causing the oil film to change its thickness. This is the reason why the exciting wedge needs to be clamped to the sample approximately 30 minutes before starting the actual measurement. This time has been determined to be sufficient to obtain neglectable influence of the contact of the exciting wedge on the measurement.

5.1.5 Post-Amplifier

The output signal of air-coupled transducer, with 2mm lift off distance of the transducer from the sample, has about 1mV peak-to-peak voltage without amplification, for the maximum Rayleigh wave amplitude, which is achievable with the transducer-wedge excitation system. The signal needs therefore to be amplified to obtain a sufficiently high signal-to-noise ratio before recording it with the oscilloscope. A Panametrics 5072PR pulser-receiver is used to amplify the signal by 40dB resulting in a peak-to-peak voltage of about 250mV.

5.1.6 Data Acquisition

The electrical output signal of the Panametrics 5072PR pulser-receiver is recorded by an oscilloscope with a sampling rate of 250 MS/s and averaged over 256 sequences. A typical 256-averaged time domain signal is depicted in Figure 5.5. In order to obtain the electrical amplitudes of the fundamental and second harmonic wave components we need to map the time domain signal (Figure 5.5) in the frequency domain. The steady state portion of the time domain signal is identified and a Hann window [25] as depicted in Figure 5.5 is applied to eliminate the ringing effects of the transducer. The obtained signal is mapped to the frequency domain using fast Fourier transform (FFT). The frequency domain signal

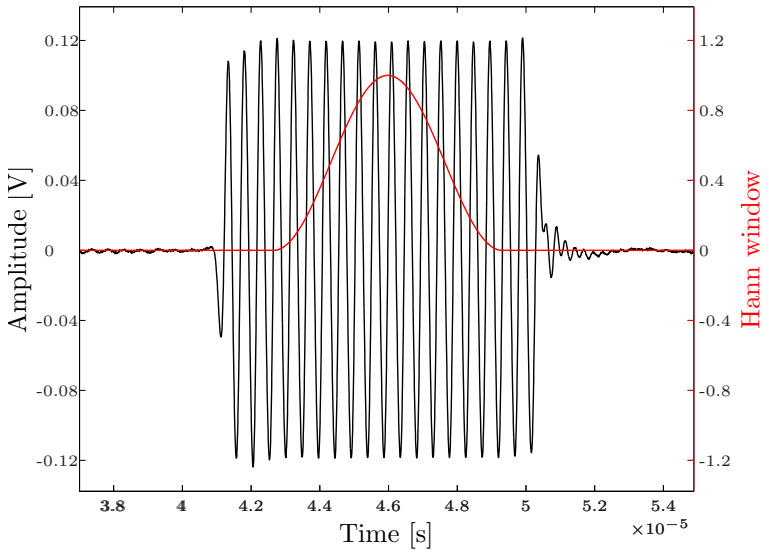

Figure 5.5: Output signal of the receiving transducer (black graph) in time domain averaged over 256 bursts and Hann (red graph) window to avoid effects of transducer ringing

is depicted in Figure 5.6, where we can clearly see the contributions of the first and second harmonic waves. Since we are not able to relate the output voltage of the transducer and the absolute particle displacement amplitude of the wave in the material, we need to introduce the obtained electrical contributions of fundamental A_1^{el} and second harmonic wave A_2^{el}.

5.2 System Nonlinearity

The electrical system used to excite the wave and detect the propagating wave is a potential source of nonlinearity, especially the amplifier and the exciting transducer can introduce higher harmonic components. The amount of second harmonic component introduced by the amplifier, the exciting transducer and the material, which are the main sources, increases with increasing excitation voltage. We can therefore conclude that a measurement of the material nonlinearity parameter, using an increasing input voltage to excite waves with different amplitudes is only valid as long as the transducer and system nonlinearity is neglectably small compared to the second harmonic generation due to material nonlinearity. As shown in Figure 5.7 a linear relationship between the squared amplitude of the fundamental wave $(A_1^{el})^2$ and the amplitude of the second harmonic A_2^{el} is measured. This

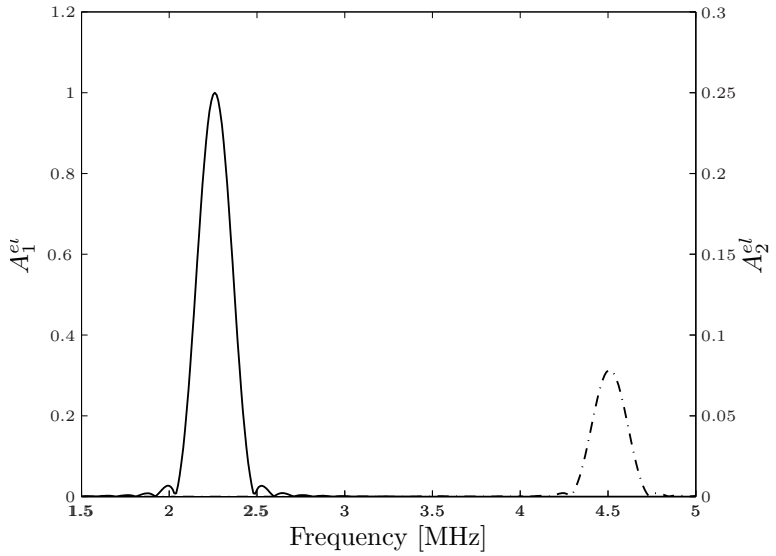

Figure 5.6: Amplitude of the electrical contribution of the first harmonic A_1^{el} (solid line) and the second harmonic wave A_2^{el} (dashed line) in the frequency domain normalized by the maximum amplitude of the first harmonic

increase consists of the contributions of the electrical system, the transducer and the material, however, the the dashed and dotted line schematically show a potential behavior of the unwanted electrical nonlinearities and the material nonlinearity can therefore not be isolated based on this data. This is the reason why a change in propagation distance using Rayleigh surface waves is useful to measure the material nonlinearity, where the second harmonic generation due to electrical devices has less influence on the measured nonlinearity parameter.

5.3 Procedure

The nonlinear Rayleigh wave measurement is performed by detecting the Rayleigh wave for increasing propagation distance because of the reasons stated in Section 5.2. The exciting wedge is clamped to the sample for one measurement set and a measurement is taken for each propagation distance by positioning the air-coupled transducer accordingly.

It has been experimentally observed with the air-coupled transducer setup that the Rayleigh wave beam, does not come straight out of the middle of the exciting wedge as depicted by the black wave field in Figure 5.8. An offset between the center line of the

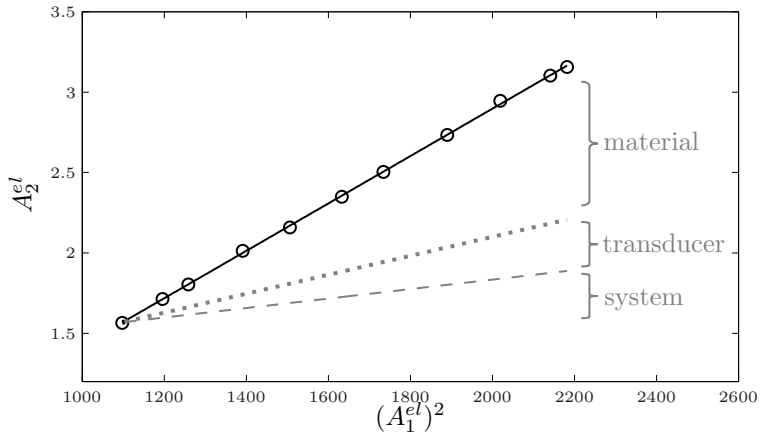

Figure 5.7: Contribution of the second harmonic wave A_2^{el} plotted over the amplitude squared of the first harmonic wave $(A_1^{el})^2$; measurement points ($\circ$) are used for the linear fit (solid line), the dashed line represents a potential contribution of second harmonic wave due to the electrical system and the dotted line the summation of both a potential system nonlinearity and a potential contribution of transducer nonlinearity

wedge and the actual middle of the wave field can be noticed as well as a small angle between the expected propagation path and the actual one. The maximum amplitude in x_3 direction of the Rayleigh wave field needs to be determined for the minimum (x_1^{min}) and maximum (x_1^{max}) propagation distance, to localize the actual path of the Rayleigh wave and reduce misalignment. The nonlinear measurements are performed along this predetermined line.

Moreover the angle between the sample and the air-coupled transducer needs to be adjusted precisely, although the angle can be calculated based on Snell's law. In practice it is useful to excite a wave, which has the frequency of the second harmonic wave in the nonlinear measurement and adjust the angle of the air-coupled transducer using this high frequency wave. The adjustment can be made based on the received signal from the transducer by looking for the angle at which the output has the highest amplitude. High frequency waves have a smaller wavelength and the angle of the air-coupled transducer is therefore more sensitive since any small angle between the plane wave propagating in air, which is leaked by the Rayleigh wave in the sample and the active area of the transducer, causes a drop in the amplitude of the received signal. The same lift-off distance between the

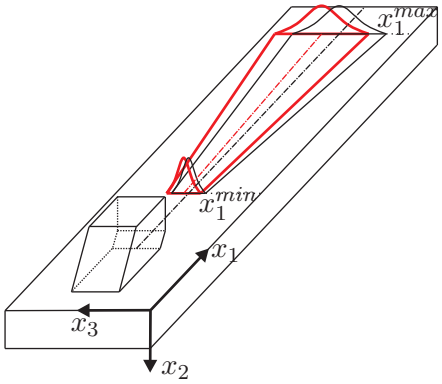

(a) Alignment procedure using the air-coupled-receiving transducer; actual (red) and expected (black) propagation path of the Rayleigh surface wave are depicted as well as the idealized Gaussian profile of the Rayleigh wave beam

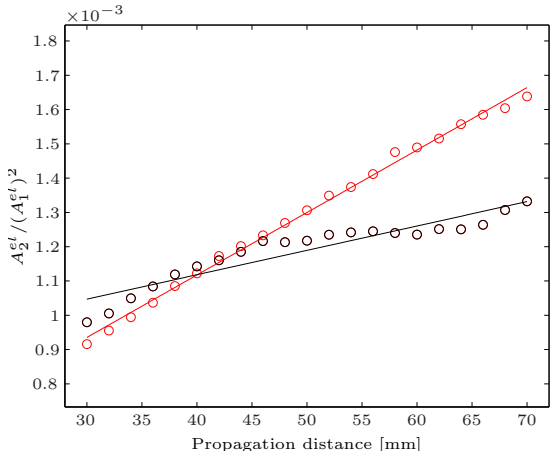

(b) $A_2^{el}/(A_1^{el})^2$ plotted over propagation distance for measurement along the actual (○) and the expected propagation path (○) as well as the best fit lines for both measurements

Figure 5.8: Alignment procedure using the air-coupled transducer

transducer and the samples is ensured by measuring the thickness of the samples precisely with a caliper and adjusting the height of the air-coupled transducer accordingly.

5.4 Processing of Nonlinear Ultrasonic Data

5.4.1 Linear Fitting

Considering equation (60), the nonlinearity parameter β is proportional to the ratio A_2/A_1^2. However, this is only valid when the propagating wave is a plane wave, where no diffraction occurs. In the three dimensional case diffraction and attenuation affect the propagating Rayleigh wave and the nonlinearity parameter is not proportional anymore. These effects can be neglected for small propagation distances and therefore a linear fitting of the obtained ratio A_2/A_1^2 over propagation distance can be used as a proper model to obtain the nonlinearity parameter, as depicted in Figure 5.9(c) by the dashed line. However, the slope of this linear fit is only proportional and not equal to the material nonlinearity parameter β because the transducer does not measure the absolute amplitude of the propagating waves, but an electric signal, which is dependent on the coupling condition, the frequency response of the transducer and in case of an air-coupled receiver, the lift off distance.

Therefore we need to introduce the nonlinearity parameter $\beta\prime$, which is calculated using the measured electrical output signal of the transducer evaluated in the frequency domain, which gives us A_1^{el} and A_2^{el}. This leads to the following relationship

$$\beta\prime \sim \frac{A_2^{el}}{(A_1^{el})^2} \sim \beta. \tag{88}$$

Therefore this research will subsequently employ the nonlinearity parameter $\beta\prime$ and the electrical contributions of the amplitudes of the first and second harmonic wave are considered A_1^{el} and A_2^{el}. The nonlinearity parameter $\beta\prime$ will therefore be only a relative measure of the material nonlinearity and be useful to compare samples. This relative measurement requires high consistency of the setup parameters throughout all measurements, which are compared with each other.

5.4.2 Diffraction and Attenuation of Rayleigh Surface Waves

The assumptions of the linear fitting model and its restriction to small propagation distances have already been discussed. Shull et al. [33] provide a model for nonlinear Rayleigh waves, which accounts for diffraction and attenuation effects. It is assumed that the wave field is generated by a line source of Gaussian amplitude distribution in the direction perpendicular to the propagation direction. The amplitude of first harmonic wave on the main axis of the Rayleigh wave beam can be written as

$$A_1(x_1) = \frac{\mathrm{i}\omega_1 A_{1,0} e^{-\alpha_1 x_1}}{\sqrt{1+\mathrm{i}x_1/\xi_1}} \exp\left[\mathrm{i}(k_1 x_1 - \omega_1 t + \varphi_{1,0})\right], \tag{89}$$

with $\xi_1 = k_1 a_s^2/2$, where a_s is the radius of the Rayleigh wave source and k_1 the wave number of the fundamental wave. The second harmonic amplitude generated by the first harmonic due to material nonlinearity is calculated using

$$\begin{aligned} A_2^M(x_1) = &- \frac{\sqrt{\pi}\beta\omega_1 A_{1,0}^2 k_1^2 a_s^2}{8c_R\sqrt{\mathrm{i}(\alpha_2-2\alpha_1)(\xi_1+\mathrm{i}x_1)}} \\ &\times \exp\left[-\alpha_2 x_1 + \mathrm{i}(\alpha_2-2\alpha_1)\xi_1\right] \\ &\times \left[\mathrm{erf}\left(\sqrt{\mathrm{i}(\alpha_2-2\alpha_1)(\xi_1+\mathrm{i}x_1)}\right) - \mathrm{erf}\left(\sqrt{\mathrm{i}(\alpha_2-2\alpha_1)\xi_1}\right)\right] \\ &\times \exp\left[\mathrm{i}(k_2 x_1 - \omega_2 t + \varphi_{2,0}^M)\right]. \end{aligned} \tag{90}$$

This line source model has shown to be an applicable model [16] for nonlinear Rayleigh waves propagating at the surface of an half space.

However to fit experimental data an extension can be made to account for the nonlinearity of the exciting transducer and the electrical system causing an initial second harmonic $A_{2,0}^T$. This effect can be modeled as an independent linear wave at the second harmonic frequency, which is diffracted and attenuated over propagation distance

$$A_2^T(x_1) = \frac{\mathrm{i}\omega_2 A_{2,0}^T e^{-\alpha_2 x_1}}{\sqrt{1+\mathrm{i}x_1/\xi_2}} \exp\left[\mathrm{i}(k_2 x_1 - \omega_2 t + \varphi_{2,0}^T)\right], \tag{91}$$

where $\xi_2 = k_2 a_s^2/2$.

Therefore the amplitude of the second harmonic wave, which is propagating in the material can be written as

$$|A_2(x_1)| = |A_2^M(x_1) + A_2^T(x_1)|. \tag{92}$$

The experimental data can be fitted based on equation (89) and (92) using the method of least nonlinear squares and the parameters α_1, α_2, $A_{1,0}$, $A_{2,0}^T$ and β are determined, the resulting curves are shown in Figure 5.9.

It has to be mentioned that the proposed model is not applicable yet to evaluate data sets, which are obtained from different samples. The number of variables (α_1, α_2, $A_{1,0}$, $A_{2,0}^T$, β), which need to be fitted is too large, causing differences of the nonlinearity parameter even for samples, which have a very similar nonlinearity parameter using the linear fitting model. However, by improving the experimental method and collecting more data points, this model can be useful to compare samples with different attenuation and to account for inherent nonlinearity.

5.4.3 Attenuation and Diffraction of Longitudinal Waves in Air

The Rayleigh wave propagating in the material is leaked to the air and the leaked longitudinal wave is detected by the air-coupled transducer. The high frequency waves, which are used for nonlinear ultrasonic measurements, are highly attenuated and the beam is diffracted while they are propagating in air. A compensation for this attenuation and diffraction is necessary, since both attenuation and diffraction are frequency dependent and therefore the

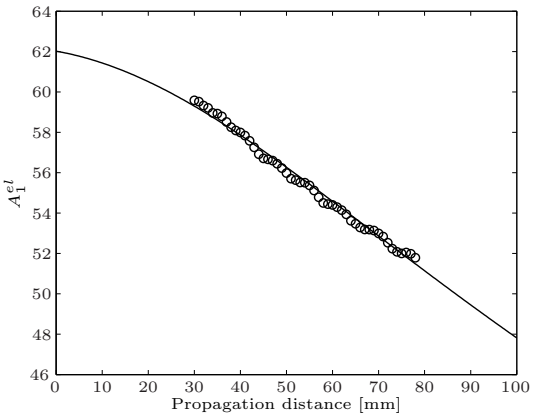

(a) Amplitude of A_1^{el} plotted over propagation distance; the theory based curve (solid line) fitted to the obtained the experimental data (∘)

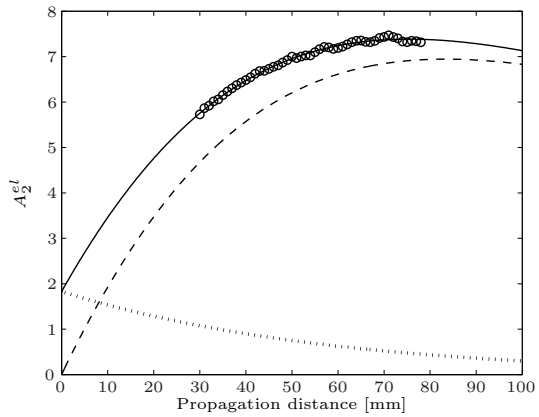

(b) Amplitude of A_2^{el} plotted over propagation distance; the theory based curve (solid line) fitted to the obtained the experimental data (∘) and is the addition of the contributions of transducer nonlinearity (dotted line) and the generated material nonlinearity (dashed line)

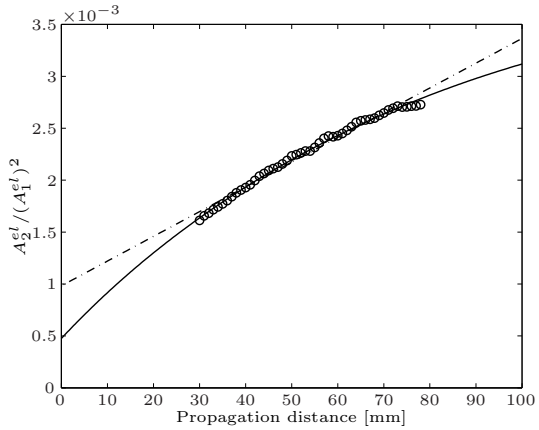

(c) Ratio $A_2^{el}/(A_1^{el})^2$ plotted over propagation distance; the curve (solid line) is calculated based on the theory based fittings in Figure (a) and (b), the linear fitting (dash-dot line) of the experimental data (∘) is shown for comparison

Figure 5.9: Theory based fitting of experimental data taking diffraction and attenuation into account and accounting for inherent nonlinearity caused by the exciting transducer and the electrical equipment

ratio A_2/A_1^2 would be affected if no compensation is performed. The leaked longitudinal wave from the sample and the air-coupled transducer can be modeled as a longitudinal wave source having a Gaussian distribution and being away from the receiving transducer by a distance l_{air} (Figure 5.10(a)). However, since the transducer has just a finite active area with a diameter d_t, we can simplify the Gaussian source by averaging over the receiving transducer diameter as depicted in Figure 5.10(b) and considering the Rayleigh wave as a uniform source.

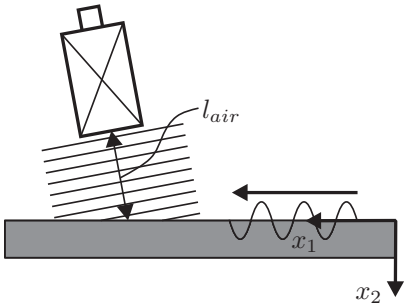

(a) Lift off distance of the air-coupled transducer

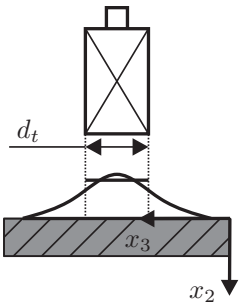

(b) Rayleigh wave beam is considered as a uniform source

Figure 5.10: Geometric aspects for the compensation of the lift off distance of the air-coupled transducer

Using this simplified model we are able to assess the attenuation and diffraction in air by applying the diffraction correction of Rogers and Van Buren [28], leading to a correction factor

$$D_L(\omega, l_{air}) = 1 - \exp\left[-\mathrm{i}\frac{2\pi}{s}\right]\left[\mathrm{J}_0\left(\frac{2\pi}{s}\right) + \mathrm{i}\mathrm{J}_1\left(\frac{2\pi}{s}\right)\right], \tag{93}$$

where

$$s = \frac{2\pi l_{air}}{k(\omega)(d_t/2)^2}, \tag{94}$$

$k(\omega)$ being the wave number of the longitudinal wave in air. The attenuation and diffraction can therefore be approximated by

$$A(\omega, l_{air}) = A(\omega, 0) D_L(\omega, l_{air}) e^{-\alpha(\omega) l_{air}}, \tag{95}$$

with $\alpha(\omega)$ being the frequency dependent attenuation coefficient.

By performing measurements for increasing propagation distance of the longitudinal wave in air, one can fit the analytical equation (95) to the data and obtain $\alpha(\omega)$, the frequency dependent attenuation coefficient.

Using 2.1 MHz as fundamental frequency, which implies 4.2 MHz to be the frequency of the second harmonic wave we obtain $\alpha(2.1\text{ MHz}) = 61.8$ Np/m and $\alpha(4.2\text{ MHz}) = 342.4$ Np/m. These results agree with the observations by Bond et al. [3] about the attenuation of high frequency ultrasonic waves in air, who provide an equation to calculate the attenuation in a frequency range above 500 kHz. This equation yields $\alpha(2.1\text{ MHz}) = 80.7$ Np/m and $\alpha(4.2\text{ MHz}) = 322.8$ Np/m and thereby shows that the measured attenuation in air agrees with the data reported in the literature. However, the measured attenuation in air for 2.1 MHz is about 18.9 Np/m lower than the value reported, but this might be caused by the fact that there is no compensation performed for temperature, humidity and pressure of the air during the measurement. In addition to that it needs to be mentioned that the validity of the averaging of the Gaussian profile needs to be investigated further and might also be a reason for the offset. However the measured value for attenuation in air of the 4.2 MHz longitudinal wave is only about 6% higher than the value reported and agrees therefore very well.

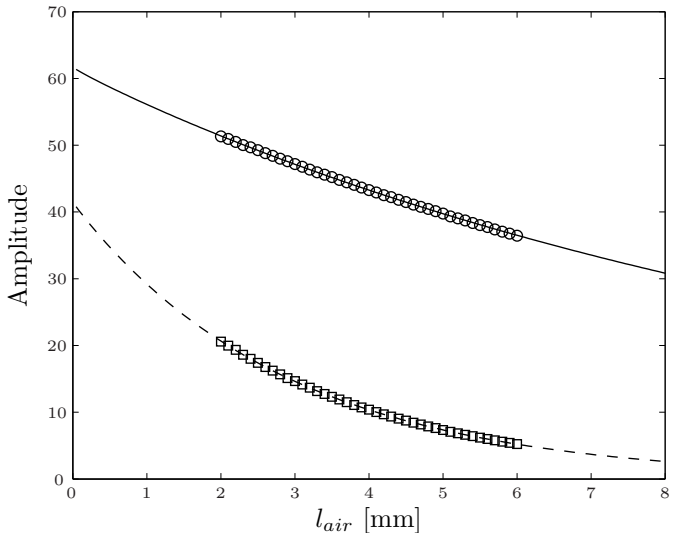

Figure 5.11: Amplitude of a 2.1 MHz wave (∘) and a 4.2 MHz (□) wave for increasing lift off distance of the air-coupled transducer and the fitted curves

Based on this measurement a correction of the nonlinear measurement for the lift off distance of the air-coupled transducer can be done, in order to compensate for the distance in air between the sample and the transducer, the equation for correction can be written as

$$A(\omega, 0) = \frac{A(\omega, l_{air})}{D_L(\omega, l_{air})} e^{\alpha(\omega) l_{air}}. \tag{96}$$

This correction factor is necessary to apply when a relation between the received output voltage from the air-coupled transducer and the Rayleigh wave amplitude has been established in order to be able to perform measurements which are independent of the lift off distance of the air-coupled transducer.

5.5 Performance of Air-Coupled-Receiver Setup

5.5.1 Comparison with Contact-Wedge-Receiver Setup

The contact-wedge-receiver setup (Figure 5.12) consists of two wedges and piezoelectric transducers which excite and receive the wave. The exciting transducer is driven at its center frequency of 2.25 MHz and the receiving narrow band transducer has a center frequency of 5 MHz.

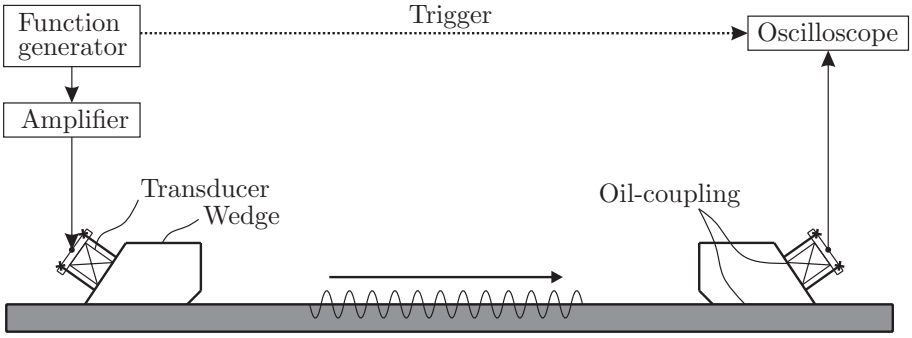

Figure 5.12: Experimental setup using contact transmitter and receiver method

The exciting wedge is fixed by a clamp at the far left side of the specimen and the receiving wedge transducer moves to the right starting from the near field distance. Each set of measurements consists of taking ultrasonic signals at 11 propagation distances. This set of measurement is repeated multiple times. After clamping the exciting wedge, it is given 30 minutes to settle since the transmission changes during that time. However it is

not feasible to wait for 30 minutes after clamping the receiving wedge since the measurement would be extremely time consuming, but the time between the application of the wedge and the actual measurement is always the same and therefore the influence on the measurement is assumed to be constant.

The variation due to the clamping of the receiving wedge is quite significant as we can see in Figure 5.13(b), where three measurement sets are performed and in each set the receiving transducer is applied for four times at each propagation distance, which adds up to twelve measurements per propagation distance in total.

Three measurement sets for increasing propagation distance are performed with the air-couple receiving transducer and the exciting wedge is reattached for each measurement set. The obtained results are depicted in Figure 5.13(a), where each point and error bar consists of three measured data points.

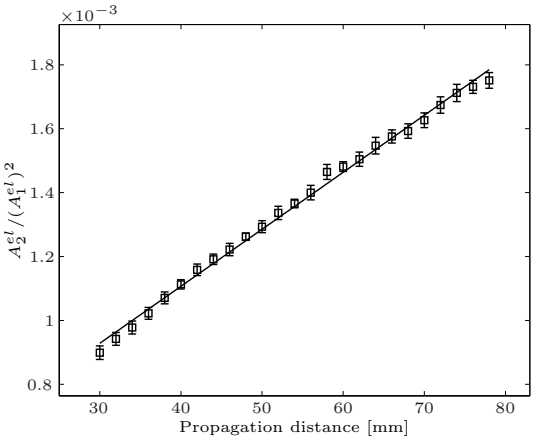

(a) Three measurement sets of $A_2^{el}/(A_1^{el})^2$ measured using the non-contact air-coupled receiving transducer plotted over propagation distance; the solid line depicts the calculated best fit line

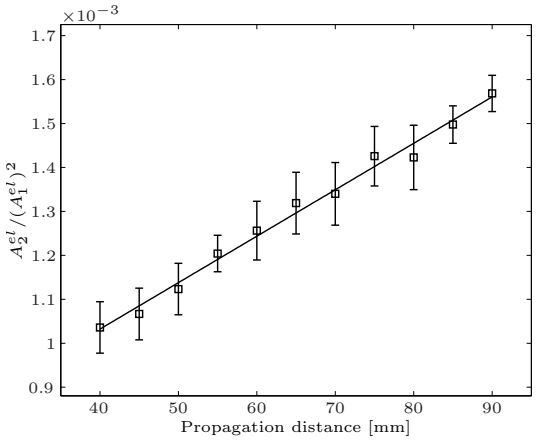

(b) Three measurement sets each consisting of four measurements per propagation distance adding up to twelve measurements of $A_2^{el}/(A_1^{el})^2$ at each propagation distance measured using the contact-wedge-receiver setup; the solid line depicts the calculated best fit line

Figure 5.13: Comparison of the repeatability of the air-coupled-receiver and contact-wedge-receiver setup; the different range of the ratio $A_2^{el}/(A_1^{el})^2$ in the two setups is caused by the different transducer characteristics and the amplification, the scale is therefore arbitrary

The standard deviation (std) of these twelve measurements from their mean value obtained with the contact-wedge-receiver setup is calculated to be about 4.65% and is therefore

relatively high compared to compared to 1.52% with the air-coupled setup. This leads to large uncertainty in the calculation of the nonlinearity parameter for the contact-wedge-receiver setup as one can see in Table 5.1. Moreover the slightly curved behavior of $A_2^{el}/(A_1^{el})^2$ which occurs due to attenuation and diffraction is discussed in Section 5.4.2 becomes obvious in the data obtained with the air-coupled receiver, whereas the variation introduced using the contact-receiver is to high to detect the slight curvature.

Table 5.1: Performance of the air-coupled-receiver setup compared to the contact-wedge-receiver setup; note that the data in this table is based on twelve measurements for each propagation distance with the contact-wedge-receiver setup and three using the air-coupled-receiver setup adding up to 132 (contact) and 72 (air-coupled) measurements per measurement set in total, the air-coupled measurement is performed from 30 mm to 78 mm propagation distance in 2 mm steps and the contact-wedge measurement from 40 mm to 90 mm in 5 mm steps

	Std from mean	Std of slope ($\beta\prime$)
Contact-wedge-receiver	4.65%	3.17%
Air-coupled-receiver	1.52%	1.08%
Relative change	−67.3%	−65.9%

5.5.2 Comparison with Absolute Nonlinearity Parameters

To validate the high performance of the air-coupled receiver setup this research performs a relative nonlinear Rayleigh surface wave measurement on two different aluminum plates (Al 2024 and Al 7075) and compare the obtained ratio of the relative nonlinearity parameters with literature data for the ratio of the absolute nonlinearity parameters determined with longitudinal waves on the same materials. The linear ultrasonic properties are assumed to be identical in both aluminum plates. The Al 2024-T351 plate used in this research is annealed at 325°C for three hours and air cooled in an uncontrolled atmosphere to remove the influence of cold work associated with the T351 tempering process. Note that the Al 7075-T651 is an aluminum plate, which is solution heat treated and artificially aged, indicated by T651. Nonlinear Rayleigh wave measurements on these Al 2024 and Al 7075 plates with 1 inch thickness are performed to obtain the relative nonlinearity parameter $\beta\prime$. Measurements are taken along two different lines on each sample to assess the spatial variation within the sample. Two representative measurements are depicted in Figure 5.14,

where one can clearly see the larger second harmonic generation of Al 7075 compared to Al 2024 which is consistent to the results of Yost et al. [40].

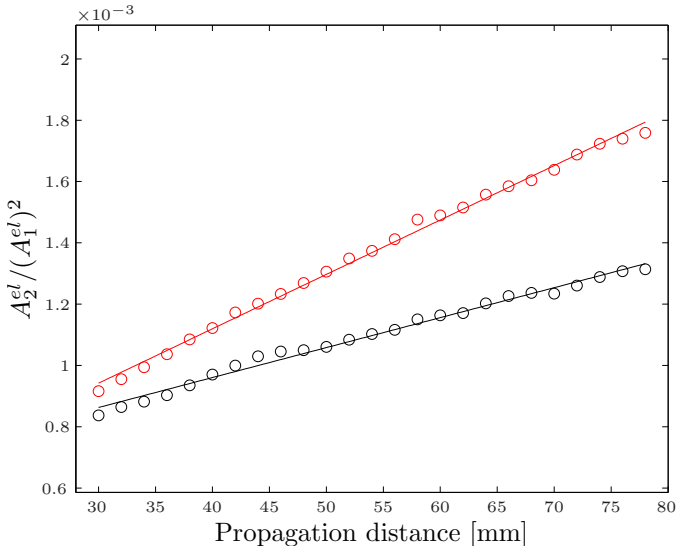

Figure 5.14: Ratio $A_2^{el}/(A_1^{el})^2$ for Al 2024 (○) and Al 7075 (○) and the best fit lines plotted over propagation distance

A spatial variation of the relative nonlinearity parameter is observed in the Al 2024 sample (±10%), however, there is only a neglectable spatial variation in Al 7075 (±1.5%) observed. Such variations can be caused by small differences in the chemical composition within the sample and different cooling rates causing differences in the microstructure.

The measured relative nonlinearity parameters $\beta\prime$ of the two aluminum plates using Rayleigh surface waves and their ratio is stated in Table 5.2. Note that the absolute non-

Table 5.2: Comparison of the ratio of the relative nonlinearity parameter $\beta\prime_{Al7075}/\beta\prime_{Al2024}$ obtained with Rayleigh surface waves and ratio of the absolute nonlinearity parameter $\beta_{Al7075}/\beta_{Al2024}$ obtained by Yost et al. [40]

Yost et al. [40]		Nonlinear Rayleigh surface wave measurement	
β_{Al7075}	7.6 ± 0.34	$\beta\prime_{Al7075}$ $(\times 10^5)$	1.7845 ± 0.0267
β_{Al2024}	4.09 ± 0.18	$\beta\prime_{Al2024}$ $(\times 10^5)$	1.0744 ± 0.0970
$\beta_{Al7075}/\beta_{Al2024}$	$2.03 - 1.70$	$\beta\prime_{Al7075}/\beta\prime_{Al2024}$	$1.85 - 1.50$

linearity measurements using longitudinal waves to assess the nonlinearity parameter performed by Yost et al. [40] suggest a ratio $\beta_{Al7075}/\beta_{Al2024}$ between 2.03 and 1.70 and the ratio obtained using the nonlinear Rayleigh surface waves yields a ratio of the relative nonlinearity parameters $\beta\prime_{Al7075}/\beta\prime_{Al2024}$ between 1.85 and 1.50. We conclude that the ob-

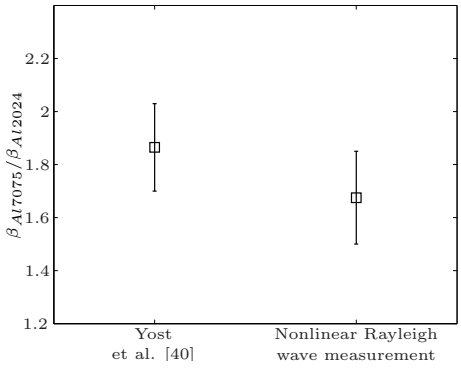

Figure 5.15: Comparison of the ratio of the obtained nonlinearity parameters for Al 2024 and Al 7075 with literature data [40]

tained results using the air-coupled-receiver setup are consistent with the results from a well-validated measurement technique [40], which demonstrates the robustness of the nonlinear Rayleigh surface wave measurement using air-coupled detection to assess the relative material nonlinearity parameter $\beta\prime$.

CHAPTER VI

EXPERIMENTAL PROCEDURE OF COMPLEMENTARY MEASUREMENTS

6.1 Longitudinal Wave Velocity Measurement

The ultrasonic velocity of a material can be measured by evaluating the first and second back wall echo from the back surface of the specimen using a longitudinal wave, which is propagating through the thickness of the material t_s as depicted in Figure 6.1. A 8.8 MHz

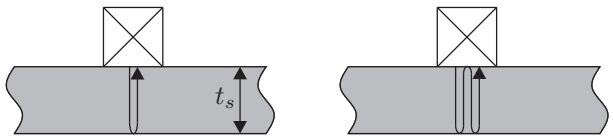

Figure 6.1: First and second back wall echo

sinusoidal excitation signal with 25 cycles and 10V peak-to-peak voltage is generated with the function generator and a half inch 10 MHz centered narrow band lithium niobate transducer is attached to the specimen using light coupling oil to introduce the longitudinal wave in the material. Consistent contact conditions throughout all measurements are ensured by giving the transducer time to settle. The wave which is propagating in the material is received with the same transducer and recorded with the oscilloscope using a sampling rate of 625 MS/s.

The velocity is calculated by performing an auto correlation of the first and second back wall echo, which essentially finds the best match of both signals, when the auto correlation reaches its maximum. The obtained time delay Δt_{12} between the signals can be used to calculate the velocity of the acoustic wave in the material

$$v_s = \frac{2t_s}{\Delta t_{12}}. \tag{97}$$

The measurement is repeated three times for each sample to avoid influence of the coupling fluid and location of the sample.

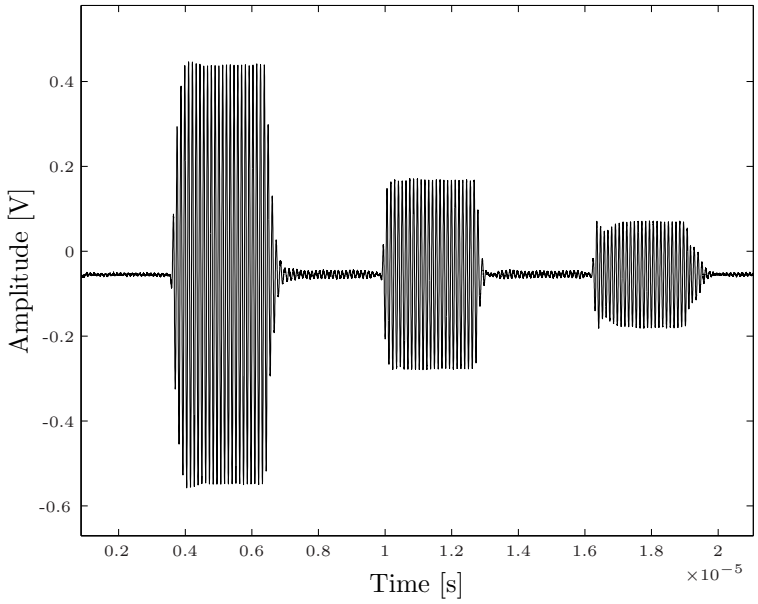

Figure 6.2: Portion of the recorded signal for the velocity calculation showing first, second and third back wall echo

6.2 Thermo-Electric Power Measurement

Thermo-electic power measurement (TEP) is done using a Koslov ThermoElectric Alloy Sorter TE-3000, which is calibrated with a Hastelloy C-276 steel probe according to the instructions of the manufacturer. After the device is turned on it needs approximately 10 minutes for the hot probe to heat up in order to obtain consistent measurements. Moreover a clean surface of the sample and the probes have to be ensured, which is done by cleaning the surfaces with acetone to remove all residues. Five measurements are done on each sample at different locations to obtain a representative value. An advantage on this technique is the independence from the sample size and also that the measurement is rapid.

The thermo-electric power measurement relies on the Seebeck effect, two probes with a certain temperature difference are connected to the sample and a difference in voltage can be measured. The Seebeck coefficient is calculated by the ratio of the difference in voltage over the difference in temperature. The voltage is dependent on the electronic scattering behavior, the electron concentration, and the effective mass of the electrons [19]. The measurement is therefore sensitive to various microstructural changes such as the solute

content of alloying elements, lattice strains, and phase changes. Most alloying elements dissolved in an iron matrix cause a decrease in the TEP value [27] as compared the TEP value of pure iron.

6.3 Microhardness Measurement

Vickers hardness measurements are performed on all samples and the obtained Vickers hardnesses are calculated by averaging over six individual measurements for each direction of the square indentation. If there is no anisotropic effect observed in these measurements the final Vickers hardness is calculated based on twelve individual measurements, six of them along the length of the sample, six along the width. The the testing parameters, a load of 2000g or 19.613N, which is applied for 10s, are kept constant throughout all measurements.

CHAPTER VII

EXPERIMENTAL RESULTS AND DISCUSSION

7.1 Complementary Measurements

7.1.1 Hardening Behavior

A clear increase in hardness with heat treatment time (Figure 7.1) is observed for 17-4 PH stainless steel specimens which are solution annealed, air cooled and subsequently heat treated (SA-AC 400-0.1, SA-AC 400-1.0, SA-AC 400-6.0). The changes agree quite well with literature data (Table 7.1). The hardness of the unaged solution annealed and air

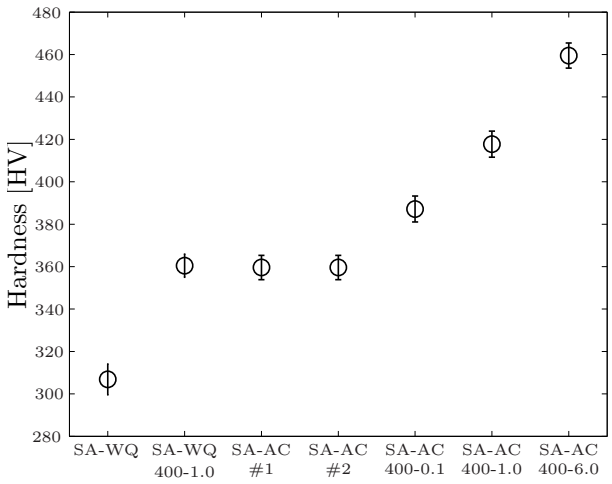

Figure 7.1: Microhardness of specimens

cooled samples (SA-AC #1 and SA-AC #2) which is approximately 360 HV is close to the 370 HV reported by Viswanathan et al. [36] for solution annealed and air cooled 17-4 PH steel. Differences in the hardness of this material with the same treatment can be caused by variations in chemical composition, mainly in the copper content and therefore slight variations in hardness between the literature data and the measured values are acceptable.

Table 7.1: Comparison of increase in hardness of the solution annealed and air cooled samples heat treated for various times with data reported by Mirzadeh et al. [23]

Sample	Temperature [°C]	Time [h]	Tempering parameter P	Measured ΔHV	Mirzadeh et al. [23] ΔHV
SA-AC #1	-	-	-	Basis for comparison	
SA-AC #2	-	-	-	0%	0%
SA-AC 400-0.1	400	0.1	11.9	8%	12%
SA-AC 400-1.0	400	1.0	13.5	16%	20%
SA-AC 400-6.0	400	6.0	14.7	28%	27%

Additionally the solution annealed and water quenched sample (SA-WQ), which is supposed to have essentially no precipitates and is therefore a good basis for comparison with literature data since the copper content has less influence on the hardness, has a measured hardness of about 307 HV, which is very close to the hardness reported by Hsaio et al. [15], who report a solution annealed and fast cooled (10 K/s) specimen with a hardness of 305 HV.

The increase in hardness of the solution annealed and water quenched sample, which is heat treated for 1h at 400°C (SA-WQ 400-1.0) compared to the water quenched sample in the unaged state (SA-WQ) is about 54 HV. A similar increase in hardness (58 HV) is also observed from the solution annealed and air cooled samples (SA-AC #1 and SA-AC #2) to the sample (SA-AC 400-1.0) which is aged for 1h at 400°C after the solution annealing and air cooling. This similar change in hardness suggests that the hardening behavior seems to be independent of the quenching after the solution annealing.

It can be concluded based on hardening mechanism of supersaturated solid solutions, as discussed by Ardell [2], that the increase in hardness with heat treatment time of the solution annealed and air cooled samples is mainly caused by the increase in number density and/or size of coherent precipitates, which cause a higher resistance for dislocations to move along their slip planes. However, plastic deformation still occurs, when the force acting on the dislocation is too large for the precipitate to sustain the force anymore causing the dislocation to break free.

The hardness of the solution annealed and water quenched sample, which is substantially lower than the hardness of the solution annealed and air cooled samples, is due to the high

cooling rate of water quenching. The solubility of copper in iron matrix is well above 3 wt.% during the solution annealing at 1040°C [32] and therefore all copper is dissolved in the austenitic matrix leading only to a transformation of the microstructure from austenite to martensite during the subsequent water quenching. The cooling rate of the quenching is high enough to avoid the diffusion of copper leading to the formation of precipitates during the process. This assumption is based on the microstrucural analysis of Hsiao et al. [15] for a fast cooled sample, where no precipitates are detected. The air cooled samples cool down slowly and thereby they are pretty long in the temperature range between 925°C, where the iron-copper solution starts to get super saturated [32] and 300°C, the temperature where the aging of 17-4 PH stainless steel is negligibly. This leads to the conclusion that there are already precipitates forming during the air cooling process, as opposed to the observations made by Rack and Kalish [26] who report a precipitate-free martensitic microstructure of the solution annealed and air cooled samples, which might be due to the limitations of the equipment in this early paper.

7.1.2 Thermo-Electric Power

The thermo-electric power measurement is sensitive to the solute contents of certain alloying elements and coherency strains as already discussed in section 6.2. We can see a clear increase (Figure 7.2) in the measured TEP values for the solution annealed and air cooled samples which were heat treated for various times (SA-AC 400-0.1, SA-AC 400-1.0, SA-AC 400-6.0). This increase is caused by the increase in volume fraction of copper rich precipitates which leads to a decrease of dissolved copper in the matrix. The same effect has already been seen by Rana et al. [27] for an interstitial-free steel forming copper precipitates. No information about the size of the precipitates or their spacing can be obtained from the TEP measurement; however, Rack and Kalish [26] suggest that the precipitation behavior of Fe-Cu-X alloys in the pre peak hardness range is similar to the precipitation behavior of a Fe-Cu binary alloy as observed by Youle and Ralph [41]. This study on Fe-Cu binary alloy suggest an approximately constant size of precipitates in the pre peak hardness range but an increasing number density with heat treatment time, causing the volume fraction of

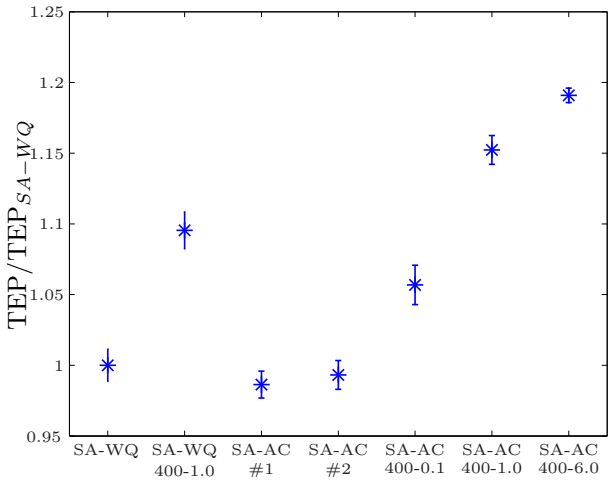

Figure 7.2: Thermo-electric power measurements on specimens thermal aged samples (normalization is done for reasons of readability, no negative thermo-electric power values occurred)

precipitates to increase.

In addition it is noticed that the increase in TEP from sample SA-AC 400-1.0 to sample SA-AC 400-6.0 is smaller than the increase from the unaged samples (SA-AC #1 and SA-AC #2) to sample SA-AC 400-0.1 and the increase from sample SA-AC 400-0.1 to sample SA-AC 400-1.0. This effect cannot be noticed in the hardening behavior (Figure 7.1) and one might conjecture that it is caused by the increasing coherency strains in sample SA-AC 400-6.0 leading to a saturation of TEP, which has already been observed by Rana et al. [27] for copper precipitation in interstitial-free steel.

The thermo-electric power value of the solution annealed and water quenched sample is similar as the solution annealed and air cooled samples which is not intuitive since the water quenching should prevent the formation of precipitates after the solution annealing because of the fast cooling rate. Therefore the measured TEP value of the water quenched sample is expected lower than the value of the air cooled samples since more copper is supposed to be dissolved in the matrix. However Viswanathan et al. [37] report that quenching of 17-4 PH from 1040°C causes probably vacancies in the lattice and these could cause an increase in thermo-electric power as investigated by Rybka and Bourassa [31] for aluminum. Nevertheless this is only a possible explanation of the obtained results and certainly further

analysis needs to be done.

Regardless of the TEP value of the sample SA-WQ, a clear increase in TEP from SA-WQ to SA-WQ 400-1.0 is observed after heat treatment for 1 hour at 400°C and therefore the behavior in TEP after heat treatment is the same as observed for the solution annealed and air cooled samples.

7.1.3 Longitudinal Wave Velocity

The measurement results of the longitudinal wave velocity (Figure 7.3) show a similar pattern as already seen in the thermo-electic power measurements (Figure 7.2), however the drop from sample SA-AC 400-1.0 to sample SA-AC 400-6.0 is not consistent with the trend of the TEP results. The similarity of the TEP and velocity measurement is probably due to

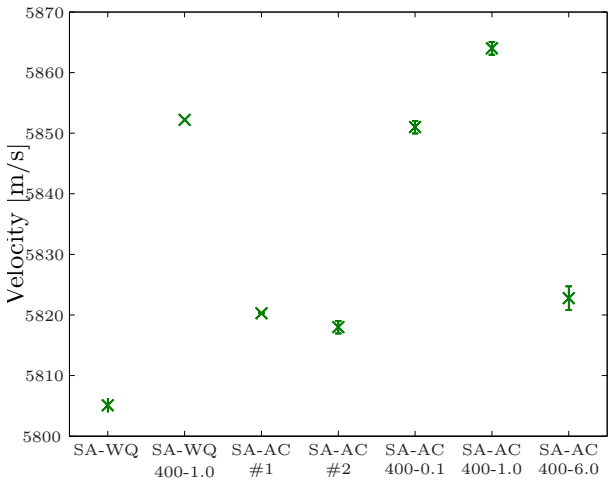

Figure 7.3: Ultrasonic velocity measurement

the fact that the velocity of sound is proportional to the elastic moduli of the material [29] and the elastic moduli are dependent on the volume fraction of precipitates. However the discrepancy between the TEP and the ultrasonic velocity measurement for sample SA-AC 400-6.0 might be explained by rate of formation of precipitates in this precipitation stage. Rosen et al. [29] suggest that the dip is occurring at the maximum rate of the formation of precipitates; this effect has been observed for aluminum alloy 2219 forming precipitates at elevated temperature. The observed dip in the change of sound wave velocity for aluminum

alloy 2219 is more pronounced for lower heat treatment temperatures and therefore the effect might also occur for 17-4 PH stainless steel, heat treated at 400°C, which is a relatively low aging temperature for this type of steel. It should be noted that the precipitation behavior of aluminum alloy 2219 and 17-4 PH stainless steel are different and the characteristics, which were seen for aluminum alloy 2219 are therefore only a possible explanation for the observed behavior of 17-4 PH stainless steel.

Table 7.2: Change in ultrasonic velocity of heat treated 17-4 PH steel samples

Sample	Ultrasonic velocity [m/s]	Relative change [%]
SA-WQ	5805.1	Basis for comparison
SA-WQ 400-1.0	5852.2	+0.81
SA-AC #1	5820.3	+0.26
SA-AC #2	5818.0	+0.22
SA-AC 400-0.1	5851.0	+0.79
SA-AC 400-1.0	5864.0	+1.01
SA-AC 400-6.0	5822.8	+0.30

The relative change in ultrasonic velocity is stated in Table 7.2 where one can note that the maximum change in ultrasonic velocity if sample SA-WQ is considered to be the base line is about 1% and this linear longitudinal wave velocity measurement is therefore insensitive to the copper precipitation of 17-4 PH stainless steel.

7.2 Nonlinear Ultrasonic Measurement

One can clearly see the decrease in nonlinearity with heat treatment time of the solution annealed and air cooled samples (SA-AC 400-0.1, SA-AC 400-1.0, SA-AC 400-6.0) in Figure 7.4. The decrease with increasing volume fraction of precipitates could be explained by a reduction of the dislocation pinning distance leading to a smaller contribution of second harmonic due to pinned dislocation based on equation (84), which is derived based on the theoretical model presented in Chapter 3. Furthermore the drop from the unaged samples (SA-AC #1 and SA-AC #2) to sample SA-AC 400-1.0 and SA-AC 400-6.0 is significant, exceeding 30% and 40% respectively and it can therefore be concluded that nonlinear ultrasound is sensitive to the mircostructural changes associated with precipitation. The

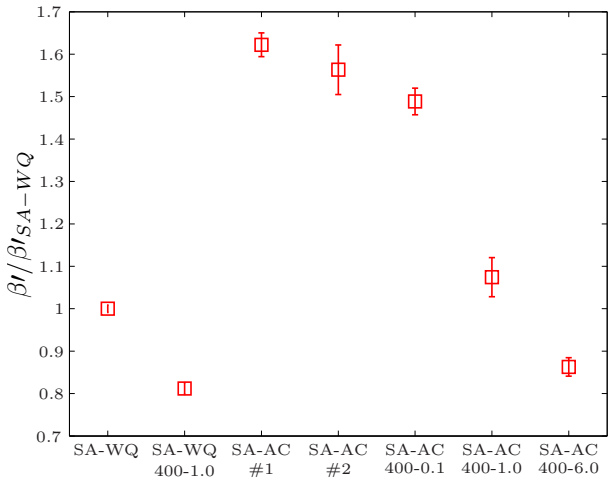

Figure 7.4: Normalized relative nonlinearity parameter obtained by nonlinear Rayleigh wave measurement using air-coupled receiver

decreasing second harmonic generation with increasing volume fraction of precipitates supports the precipitation characteristics suggested by Rack and Kalish [26] who assume that the precipitation behavior of Fe-Cu-X alloys in the pre peak hardness range is similar to Fe-Cu binary alloys as observed by Youle and Ralph [41], namely relatively constant size of precipitates and increasing number density.

About 10% difference in nonlinearity is observed between specimen SA-AC #1 and SA-AC #2, which are both in the same unaged condition. This difference indicates that the variation between two samples in the same state is not insignificant, but small compared to the changes associated with thermal aging.

Moreover there is a large increase in nonlinearity observed from sample SA-WQ to the samples SA-AC #1 and SA-AC #2, which is reasonable since the water quenching should prevent the formation of copper rich precipitates and there should be no pinning of dislocations due to precipitates in the solution annealed and water quenched sample.

However, aging of a solution annealed and water quenched sample does not lead to an increase in nonlinearity but a decrease in second harmonic contribution, as one can observe by comparing the unaged specimen SA-WQ and sample SA-WQ 400-1.0, which was aged for 1h at 400°C. An increase would have been expected assuming no precipitates

in the water quenched sample and weak pinning effects by grain boundaries and other microstructural arrangements. However, the measured decrease might be explained by the already discussed possibility of quenched in vacancies, which are annealed out during the heat treatment at 400°C. Therefore the decrease in second harmonic generation might be caused by a superposition of the formation of precipitates and the anneal of vacancies. But this hypothesis needs to be investigated further since neither the strength of vacancies to pin dislocations nor their density in the water quenched sample is known.

7.3 Mircostructural Interpretation

It is observed that both the hardness and termo-electric power increase with aging time for the solution annealed and air cooled samples; these effects are caused by the formation of copper rich precipitates. The relative increase in hardness and TEP agrees very well for specimens SA-AC 400-0.1 and SA-AC 400-1.0, whereas a saturation effect in the thermo-electric power for the sample SA-AC 400-6.0 is noticeable, which does not occur in the hardness as one can see in Figure 7.5(b). This saturation might be affected by increasing coherency strains in the martensitic matrix leading to a decrease of TEP superimposed on the increase of TEP due to decreasing solute content of copper.

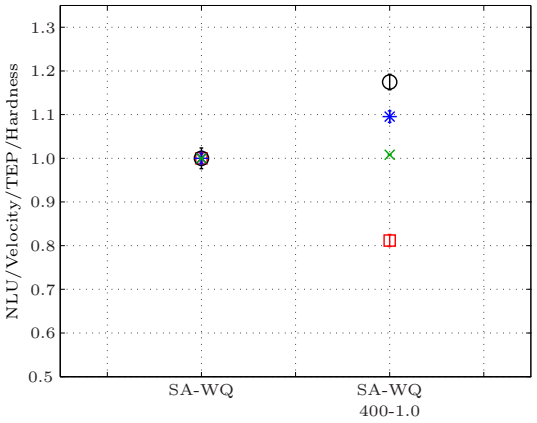

(a) Solution annealed and water quenched sample in reference and heat treated condition normalized by the value of sample SA-WQ

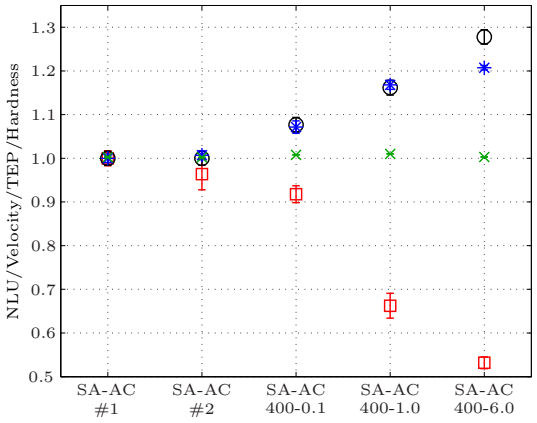

(b) Solution annealed and air cooled samples heat treated for various times normalized by the value of sample SA-AC #1

Figure 7.5: Comparison of nonlinear ultrasonic measurement (□), hardness (○), longitudinal ultrasonic velocity (×) and thermo-electric power measurements (∗)

The increasing volume fraction can be assumed to be mainly due to an increasing number density of precipitates and relatively constant size of precipitates as suggested by Rack and Kalish [26] for 17-4 PH stainless steel, similar to the behavior reported by Youle and Ralph [41] for Fe-Cu binary alloy. This agrees well with the observed decreasing second harmonic generation with increasing heat treatment time of the solution annealed and air cooled samples and therefore the dislocation pinning distance is likely to be reduced.

In addition a significantly lower nonlinearity parameter is observed for the unaged water quenched sample SA-WQ compared to the unaged solution annealed and air cooled samples (SA-AC #1 and SA-AC #2), which is likely due to the water quenching, which prevents the formation of precipitates, leading to a large decrease of precipitate number density and size compared to the air cooled samples.

The lower relative nonlinearity parameter, observed for the solution annealed and water quenched samples, which is heat treated for 1 h at 400°C as compared to that for the unaged sample (SA-WQ) might be caused by an anneal-out of the quenched-in vacancies during the heat treatment at 400°C and the formation of precipitates, but this hypothesis needs to be investigated further.

It needs to be mentioned that the observed changes in ultrasonic velocity give mainly information about the volume fraction of precipitates as the thermo-electric power does. However, the maximum difference between two samples is about 1% and therefore the measurement is not sensitive enough to the microstructural changes, which is as shown in Figure 7.5, where the relative changes in ultrasonic velocity are negligible as compared to changes in thermo-electric power, hardness and nonlinear ultrasound.

CHAPTER VIII

CONCLUSIONS AND OUTLOOK

This research demonstrates an accurate and flexible technique using an air-coupled non-contact receiving transducer to perform nonlinear Rayleigh wave measurements. The experimental setup and procedures are described. A comparison with the contact-wedge-receiver method for nonlinear Rayleigh waves in terms of accuracy is made and the results of the air-coupled receiving setup are validated using literature data. The data of this accurate measurement technique is further used to take into account diffraction and attenuation effects involved in the measurement technique. In addition the inherent nonlinearity of electronic devices is also accounted for to improve the assessment of the material nonlinearity contribution. This data processing is promising to perform nonlinear Rayleigh wave measurements for longer propagation distances, where the linear fitting is less accurate because of the attenuation effects and to compare samples with different attenuation.

Furthermore a comprehensive explanation of the second harmonic generation due to coherent precipitates is given, which relates microstructural features to the contribution in nonlinearity of pinned dislocations. A short overview of the theoretical background of precipitation in supersaturated solid solutions is provided to enable the reader to follow the thermal treatment which the specimens of this research are exposed to.

Thermal aging for various heat treatment times of 17-4 PH stainless steel specimens is performed to enhance the diffusion of alloying elements in the martensitic microstructure and to obtain samples in different precipitation stages, which are measured using nonlinear Rayleigh surface waves. The results suggest an increasing second harmonic contribution in early stages of precipitation, which was investigated by comparing a solution annealed and water quenched sample with a solution annealed and air cooled sample. Moreover a decrease in nonlinearity after the heat treatment of solution annealed and air cooled samples is observed and this effect might be mainly caused by the reduction of the pinning distance

of dislocations, which will suppress the second harmonic generation.

Thermo-electric power, microhardness and ultrasonic velocity measurements are performed additionally to support the obtained nonlinear ultrasonic data and help interpret the precipitation characteristics. These measurements clearly suggest an increase in volume fraction of precipitates with heat treatment time. Especially the hardness agrees very well with already existing literature data. However, the trend of longitudinal wave velocity measurements is not in complete agreement with those of thermo-electric power or hardness measurements and are insensitive to the microstructural changes.

Further work needs to be done to fully characterize the air-coupled transducer in terms of relating the output voltage to the absolute displacement of the wave in the material. This would enable performing an absolute nonlinear measurement and measuring the acoustic nonlinearity parameter β. Moreover an accurate measurement of the attenuation coefficients of first and second harmonic waves for the diffraction and attenuation model would reduce the variables which are needed for fitting to the data, thus the independent measurements would improve the calculation of the nonlinearity parameter.

The second harmonic generation due to precipitation in 17-4 PH stainless steel has only been investigated in the pre-peak hardening stages in this research and therefore further work needs to be done to fully characterize the second harmonic generation, especially in the stages where precipitates start to loose coherency and in the over-aged stage. All changes in the microstructure of the precipitate hardenable steel are just observed by macroscopic measurements, although nonlinear ultrasound is very sensitive to microstrucutral changes, optical analysis with high-resolution microscopes of the samples would help to further validate the underlying theoretical model and the obtained data.

REFERENCES

[1] Achenbach, J. D., *Wave Propgation in Elastic Solids*. Amsterdam: North-Holland Pub. Co., 1973.

[2] Ardell, A. J., "Precipitation hardening," *Metallurgical and Materials Transactions*, vol. 16, pp. 2131–2165, 1985.

[3] Bond, L. J., Chiang, C.-H., and Fortunko, C. M., "Absorption of ultrasonic waves in air at high frequencies (10-20 mhz)," *Journal of the Acoustical Society of America*, vol. 92, no. 4, pp. 2006–2015, 1992.

[4] Cantrell, J. H., "Fundamentals and applications of nonlinear ultrasonic nondestructive evaluation," in *Ultrasonic Nondestructive Evaluation* (Kundu, T., ed.), CRC Press, 2004.

[5] Cantrell, J. H., "Substructural organization, dislocation plasticity and harmonic generation in cyclically stressed wavy slip metals," *Proceedings of the Royal Society London*, pp. 757–780, 2004.

[6] Cantrell, J. H. and Yost, W. T., "Effect of precipitate coherency strains on acoustic harmonic generation," *Journal of Applied Physics*, vol. 81, pp. 2957–2962, 1997.

[7] Cantrell, J. H. and Zhang, X.-G., "Nonlinear acoustic response from precipitate-matrix misfit in a dislocation network," *Journal of Applied Physics*, vol. 84, pp. 5469–5472, Nov. 1998.

[8] Christien, F., Telling, M. T. F., and Knight, K. S., "Neutron diffraction in situ monitoring of the dislocation density during martensitic transformation in a stainless steel," *Scripta Materialia*, vol. 68, pp. 506–509, 2013.

[9] Cobb, A., Capps, M., Duffer, C., Feiger, J., Robinson, K., and Hollingshaus, B., "Nonlinear ultrasonic measurements with emats for detecting pre-cracking fatigue damage," *AIP Conference Proceedings*, vol. 31, pp. 299–306, 2012.

[10] Graff, K. F., *Wave Motion in Elastic Solids*. New York: Dover, 1991.

[11] Hamilton, M. F. and Blackstock, D. T., *Nonlinear Acoustics*. San Diego, CA: Academic Press, 1998.

[12] Herrmann, J., Kim, J.-Y., Jacobs, L. J., Qu, J., and Littles, J. W., "Assessment of material damage in a nickel-base superalloy using nonlinear rayleigh surface waves," *Journal of the Acoustical Society America*, vol. 120, pp. 1266–1273, 2006.

[13] Hikata, A., Chick, B. B., and Elbaum, C., "Dislocation contribution to the second harmonic generation of ultrasonic waves," *Journal of Applied Physics*, vol. 36, p. 229, 1965.

[14] Hollomon, J. H. and Jaffe, J. D., "Time-temperature relations in tempering steel," *Trans. Amer. Inst. Min. Metall. Eng.*, vol. 162, p. 223, 1945.

[15] Hsiao, C. N., Chiou, C. S., and Yang, J., "Aging reactions in a 17-4 ph stainless steel," *Material Chemistry and Physics*, vol. 74, pp. 134–142, 2002.

[16] Huang, C.-L., "Effect of beam diffraction on nonlinear rayleigh surface wave measurement," Master's thesis, Georgia Institute of Technology, May 2013.

[17] Hurley, D. C., "Nonlinear propagation of narrow-band rayleigh wave excited by a comb transducer," *Journal of the Acoustical Society of America*, vol. 106, pp. 1782–1788, 1999.

[18] Hurley, D. C., Balzar, D., and Purtscher, P. T., "Nonlinear ultrasonic assessment of precipitation hardening in astm a710 steel," *Journal of Materials Research*, vol. 15, pp. 2036–2042, Nov. 2000.

[19] Lara, N. O., Ruiz, A., Rubio, C., Ambriz, R. R., and Medina, A., "Nondestructive assessing of the aging effects in 2205 duplex stainless steel using thermoelectric power," *NDT&E International*, vol. 44, pp. 463–468, 2011.

[20] Liu, M., Kim, J.-Y., Jacobs, L. J., and Qu, J., "Experimental study of nonlinear rayleigh wave propagation in shot-peened aluminum plates - feasibility of measuring residual stress," *NDT&E International*, vol. 44, pp. 67–74, 2011.

[21] Martin, J. W., *Precipitation Hardening*. Butterworth Heinemann, second ed., 1998.

[22] Matlack, K. H., Wall, J. J., Kim, J.-Y., Qu, J., Jacobs, L. J., and Viehrig, H.-W., "Evaluation of radiation damage using nonlinear ultrasound," *Journal of Applied Physics*, vol. 111, 2012.

[23] Mirzadeh, H. and Najafizadeh, A., "Aging kinetics of 17-4 ph stainless steel," *Material Chemistry and Physics*, vol. 116, pp. 119–124, 2009.

[24] Odette, G. R. and Lucas, G. H., "Embrittlement of nuclear reactor pressure vessels," *JOM*, vol. 53, pp. 18–22, 2001.

[25] Oppenheim, A. V. and Schafer, R. W., *Discrete-time signal processing*. Upper Saddle River, NJ: Prentice Hall, second ed., 1999.

[26] Rack, H. J. and Kalish, D., "The strength, fracture toughness, and low cycle fatigue behavior of 17-4 ph stainless steel," *Metallurgical Transactions*, vol. 5, pp. 1595–1605, 1974.

[27] Rana, R., Singh, S. B., and Mohanty, O. N., "Thermoelectric power studies of copper precipitation in a new interstitial-free steel," *Scripta Materialia*, vol. 55, pp. 1107–1110, 2006.

[28] Rogers, P. H. and Buren, A. L. V., "An exact expression for the lommel diffraction correction integral," *Journal of the Acoustical Society of America*, vol. 55, pp. 724–728, 1974.

[29] Rosen, M., Horowitz, E., Fick, S., Reno, R. C., and Mehrabian, R., "An investigation of the precipitation-hardening process in aluminum alloy 2219 by means of sound wave velocity and ultrasonic attenuation," *Materials Science and Engineering*, vol. 53, pp. 163–177, 1982.

[30] Ruiz, A., Ortiz, N., Medina, A., Kim, J.-Y., and Jacobs, L. J., "Application of ultrasonic methods for early detection of thermal damage in 2205 duplex stainless steel," *NDT&E International*, vol. 54, pp. 19–26, 2013.

[31] Rybka, T. and Bourassa, R. R., "Thermoelectric power of vacancies in aluminum," *Physical Review B*, vol. 8, pp. 4449–4457, Nov. 1973.

[32] Salje, G. and Feller-Kniepmeier, M., "The diffusion and solubility of copper in iron," *Journal of Applied Physics*, vol. 45, pp. 1833–1839, May 1977.

[33] Shull, D. J., Kim, E. E., and Zabolotskaya, M. F. H. E. A., "Diffraction effects in nonlinear rayleigh wave beams," *Journal of the Acoustical Society of America*, vol. 97, pp. 2126–2137, 1995.

[34] Valluri, J. S., Balasubramaniam, K., and Prakash, R. V., "Creep damage characterization using non-linear ultrasonic techniques," *Acta Materialia*, vol. 58, pp. 2079–2090, 2010.

[35] Viswanath, A., Rao, B. P. C., Mahadevan, S., Jayakumar, T., and Raj, B., "Mircostructural characterization of m250 grade maraging steel using nonlinear ultrasonic technique," *Journal of Materials Science*, vol. 45, pp. 6719–6726, 2010.

[36] Viswanathan, U. K., Banerjee, S., and Krishnan, R., "Effects of aging on the microstructure of 17-4 ph stainless steel," *Material Science and Engineering*, vol. 104, pp. 181–189, 1988.

[37] Viswanathan, U. K., Nayar, P. K. K., and Krishnan, R., "Kinetics of precipitation in 17-4 ph stainless steel," *Material Science and Technology*, vol. 5, pp. 346–349, 1989.

[38] Walker, S. V., "Characterization of fatigue damage in a36 steel specimens using nonlinear rayleigh surface waves," Master's thesis, Georgia Institute of Technology, 2011.

[39] Walker, S. V., Kim, J.-Y., Qu, J., and Jacobs, L. J., "Fatigue damage evaluation in a36 steel using nonlinear rayleigh surface waves," *NDT&E International*, vol. 48, pp. 10–15, 2012.

[40] Yost, W. T. and Cantrell, J. H., "Effects of artificial aging of aluminum 2024," in *Review of Progress in Nondestructive Evaluation* (Thomson, D. O. and Chimenti, D. E., eds.), vol. 12, pp. 2067–2073, New York: Plenum Press, 1993.

[41] Youle, A. and Ralph, B., "A study of the precipitation of copper from α-iron in the pre-peak to peak hardness range of aging," *Metal Science Journal*, vol. 6, pp. 149–152, 1972.

[42] Zeitvogel, D. T., "Characterization of damagedue to stress corrosion cracking in carbon steel using nonlinear rayleigh surface acoustic waves," Master's thesis, Georgia Institute of Technology, 2012.